Renewable and Sustainable Energy Reviews 27 (2013) 334–349

Contents lists available at SciVerse ScienceDirect

Renewable and Sustainable Energy Reviews

journal homepage: www.elsevier.com/locate/rser

Review on nanostructured photoelectrodes for next generation dye-sensitized solar cells

José Maçaira, Luísa Andrade, Adélio Mendes *

LEPAE—Departamento de Engenharia Química, Universidade do Porto—Faculdade de Engenharia, Rua Dr. Roberto Frias, s/n 4200-465 Porto, Portugal

A R T I C L E I N F O

Article history:
Received 5 November 2012
Received in revised form
2 July 2013
Accepted 5 July 2013
Available online 27 July 2013

Keywords:
Dye-sensitized solar cells
Nanoparticles
Photoelectrode
Electron transport
Recombination
Graphene

A B S T R A C T

This work reviews the state-of-the-art nanostructured photoelectrodes for use in dye-sensitized solar cells. The influence of the photoelectrode structure in the DSC performance is analyzed. The nanostructured photoelectrodes can be classified into: (1) nanoparticles with high surface areas for efficient dye loading; (2) 1D nanostructures such as nanotubes and nanowires that offer direct electron transport pathways towards the collecting substrate; (3) 3D hierarchically ordered photoelectrodes that combine large pores for efficient electrolyte diffusion, large particles for effective light scattering but also small particles needed to achieve high surface areas; (4) 3D template-based techniques that create highly conductive macroporous scaffolds to produce structures with different length scales for electrolyte diffusion (macro and mesopores) and dye loading (micro and nanopores); and finally (5) hybrid TiO_2/graphene nanostructures able to suppress electron recombination in the semiconductor/electrolyte interface, increasing the electron mobility and extraction and also able to enhance light absorption, ultimately increasing the DSC performance.

Contents

1. Introduction

World energy consumption will increase 53% before 2035, driven not only by the economic growth and increasing population in developing countries but also by emerging economies such as China and India [1]. Relatively high oil prices, as well as concerns about the environmental impact of the fossil fuels combustion and strong government incentives have made renewables the fastest growing energy source according to the International Energy Outlook of 2011. The total renewable energy generation has increased 3.1% per year and it is expected to grow from 19%, recorded in 2008, to 23% in 2035 [2]. In particular, solar energy is the fastest growing segment of renewable energy sources, which in the non-OECD countries is expected to grow annually 22.8% until 2035. The forecasts for 2015 put total installed photovoltaic (PV) capacity in the world between 131 GW and 196 GW; 100 GW could be reached in 2013 [2].

Obviously, the PV market evolution will make use of the most competitive solar panels at the time, most likely the first

* Corresponding author. Tel.: +351 91 9889237.
E-mail address: mendes@fe.up.pt (A. Mendes).

1364-0321/$ - see front matter
http://dx.doi.org/10.1016/j.rser.2013.07.011

Nomenclature

V_{oc}	Open-circuit voltage, V
FF	Fill factor
I_s	Incident photon flux, $m^2\ s^{-1}$
J_{sc}	Short circuit current density, $A\ m^{-2}$
D_{eff}	Diffusion coefficient of electrons, $m^2\ s^{-1}$
L_f	Thickness of the TiO_2 film, m
L_n	Diffusion length, m
R_k	Recombination resistance, Ω
R_w	Transport resistance, Ω
FTO	Fluorine-doped SnO_2 conducting glass electrode
C_μ	Chemical capacitance
CB	Conduction band

Greek letters

η	Efficiency
α	Wavelength-dependent absorption coefficient, m^{-1}
τ_{e^-}	Electron lifetime, s
τ_{tr}	Electron transport time, s
η_{cc}	Collection efficiency

Subscripts

e^-	Electrons
I^-	Iodide
I_3^-	Triiodide
MPP	Maximum power point
OC	Open circuit
SC	Short-circuit

generation crystalline and polycrystalline silicon solar panels (c-Si). These devices at lab scale can achieve up to 25% sun to power conversion efficiency (PCE, η) and their recent progressively lowering prices reflects its industrial establishment that, undoubtedly, makes use of the today′s semiconductor industry infrastructures. However, the high production and environmental costs led to a constant progress in the development and establishment of new PV technologies aiming to avoid the drawbacks of the c-Si solar panels. Some established semiconductor based technologies comprise gallium arsenide tin film solar cells (GaAs, $\eta\approx24\%$), copper–indium–galium–diselenide (CIGS, $\eta\approx20\%$), cadmium–telluride (CdTe, $\eta\approx17\%$) and amorphous/nanocrystalline silicon ($\eta\approx10\%$) solar cells [3]. This second generation of thin film technologies are believed to have an important role in the PV installation capacity by 2015 [2]. However, they also share the same performance and cost limitations as conventional Si devices. After approximately 20 years of research and development, third generation thin film solar devices are starting to emerge in the marketplace. This new generation of photovoltaic systems includes semiconductor quantum dots (QDPV, $\eta\approx6$–10%) [4], organic semiconductors (OPV, $\eta\approx10\%$) [3,5] and dye sensitized solar cells (DSCs, $\eta\approx13\%$) [6]. These new technologies benefit from their low processing costs and environmental impact and thus short payback time when compared to the conventional solar devices. At present stage, third generation PV technologies are still far behind the efficiency values of the conventional Si-based solar cells (~20%); nevertheless, the promise of low processing costs and usage of available environmental-friendly raw materials make them subject to an intensive research and development.

Dye sensitized solar cells present themselves as a very promising photovoltaic technology. They are made of cheap components that are non-toxic and world-wide available and offer distinctive features such as semi-transparency, multi-color range possibilities, flexibility and lightweight applications but also good performance under low light conditions and different solar incident angles [7–9]. These unique characteristics open a new possibility of applications and markets where conventional solar devices will never be able to penetrate, *e.g.* low-power consumer electronics, outdoor or indoor recreational and BIPV applications. In fact, the DSC technology has recently been used by several companies in some commercial applications by Sony, Fujikura, Panasonic, G24i, Dyesol, 3G Solar and Toyota-Asin. However, for the DSC technology become a competitive alternative to the present PV technologies, major breakthroughs are necessary mainly concerning the two critical aspects of any PV device: power conversion efficiency and lifetime. Regarding the device lifetime, at least 25 years of constant power conversion efficiency should be guaranteed for outdoor applications. This aspect has caught researcher′s attention in order to enhance DSCs′ stability and thus many reports are being published concerning improvements on the stability devices and new sealing methods [10–15]. Several methods were proposed to enhance the efficiency of DSCs [6,16–18] being one of the most promising the use of nanostructured materials as photoelectrodes to enhance light harvesting and charge extraction to improve photocurrent, photovoltage and fill factor.

This work aims to review the state-of-the-art DSCs and mostly to demonstrate the influence of the photoelectrode structure in the DSC performance. Particular emphasis is given to nanostructured materials and cells, as well as their synthesis methods. This review discusses the various advantages of nanostructured DSC cells and the fact that a tailored design of the photoelectrode structure is crucial to control the charge extraction, to enhance light harvesting and to reduce charge recombination.

2. Operational principle of dye sensitized solar cells

In 1991 O′Regan and Grätzel proposed the first bulk heterojuntion photoelectrochemical solar cell with 7% power conversion efficiency, taking advantage of the 3D TiO_2 photoelectrode film and using a ruthenium dye as sensitizer [19]. DSCs mimic natural photosynthesis and differ from conventional p–n junction devices because light collection and charge transport are separated in the cell. Light absorption occurs in the chemisorbed sensitizer molecule, while electron transport occurs in the semiconductor anatase TiO_2—Fig. 1.

The photoelectrode is a mesoporous oxide layer composed of nanometer-sized particles. Attached to the surface of the oxide is a monolayer of dye responsible for light absorption. The optical absorbance that occurs in the dye molecules results in excitation of an electron from the highest occupied molecular orbital (HOMO) to the lowest unoccupied molecular orbital (LUMO) [20]. The photogenerated electrons are transferred to the conduction band of the semiconductor oxide and percolate through the

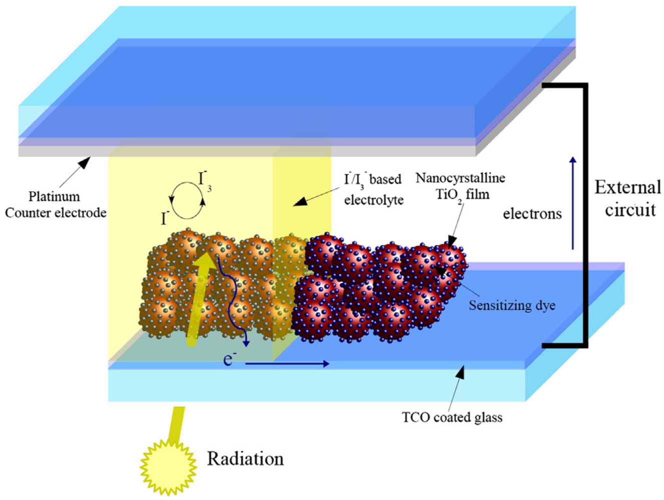


Fig. 1. Schematic diagram of the working principles of a dye sensitized solar cell.

semiconductor network, being collected at the transparent conducting oxide. The oxidized dye is regenerated by electron donation from the electrolyte solution containing a redox couple, typically of iodide/triiodide. The triiodide ions formed in the semiconductor′s surface during the redox reaction diffuse to the Pt-catalyzed counter-electrode, where they are reduced back to iodide by the electrons from the external circuit. The PCE of the solar cell is determined by its current–voltage characteristics, specifically the open-circuit photovoltage (V_{oc}), the photogenerated current density measured under short-circuit conditions (J_{sc}), light irradiance (I_s) and the fill factor of the cell (FF), which depends on the series resistances and on the shunt resistances in the cell [21]:

$$\eta_{\text{global}} = \frac{J_{sc} V_{oc}}{I_s} FF \tag{1}$$

The short-circuit photocurrent (J_{sc}) is essentially related to the amount of sunlight harvested in the visible part of the solar spectrum by the sensitizer. Consequently, dye molecules play a critical role in photon capture and for this reason the progress in DSCs have been closely followed by the constant development of new porphyrin and organic D-π-A sensitizers that have high extinction coefficients and broader optical absorption spectra. These have even supplanted the commonly used Ru(II) polypyridil sensitizers in liquid but also in solid-state electrolyte DSCs [6,10,22–30].

The open-circuit voltage (V_{oc}) is related to the energy difference between the quasi-Fermi level of electrons in the semiconductor and the chemical potential of the redox mediator in the electrolyte [31]. The most common electrolyte in high performance DSCs uses the triiodide/iodide (I_3^-/I^-) redox couple [22,32,33]. Despite the excellent results achieved so far using this redox couple, it presents some drawbacks such as the corrosion of several current collectors and partial absorption of visible light around 430 nm, resulting in a voltage loss [34]. To mitigate these effects several alternatives are been studied [30,35–38]. Good results have been reported using an amorphous organic hole-transport material (HTM), spiro-OMeTAD (2,2′,7,7′-tetrakis(*N*,*N*-di-*p*-methoxyphenyl-amine)9,9′-spirobifluorene) [39] and cobalt based (Co (II/III) tri(bypiridyl)) non-corrosive electrolyte. These new hole transport materials yielded impressive results, reaching PCEs higher than 12% and V_{oc} of 925 mV for liquid-state DSCs and 7.2% and 965 mV for solid-state devices [6,39–45]. Other materials like processable p-type direct bandgap semiconductor $CsSnI_3$ have been used very recently for hole conduction, aiming to replace the liquid iodide/triiodide based electrolyte. This hole conductor yielded record efficiencies of 8.5% for solid state DSCs [46]. A very interesting and underexplored class of materials of organometallic halide perovskite have also been used as sensitizers in liquid electrolyte-based photoelectrochemical cells with conversion efficiencies from 3.5 to 6.5% [47,48]. These materials provide excellent support for binding organic and inorganic components to form a molecular composite that not only acts as a sensitized, but also as a hole and electron conductor. Recently $CsSnI_3$ perovskite was shown to be an efficient hole conductor in a solid state DSC originating a cell that achieved 8.5% efficiency [46]. Another specific perovskite, a methylamonium lead iodide chloride ($CH_3NH_3PbI_2Cl$), was used as the light absorbing material in conjunction with TiO_2 as transparent n-type component; holes were transported from the perovskite surface to the counter-electrode using a layer of spiro-OMeTAD; the device achieved 8% efficiency [49]. Interestingly, the authors found that by replacing TiO_2 photoelectrode by an insulating framework of AlO_3 the conversion power efficiency improves to almost 11%. Apparently the perovskite material employed is a much better electron conductor than TiO_2 photoelectrode, and the AlO_3 only acted as a "scaffold" to support and provide surface area to the perovkite to be coated on. Other record-breaking work proposed an innovative platform that includes a three dimensional nanocomposite and bilayer architecture with an inorganic–organic hybrid heterojuntion [50]: the use of $TiO_2/CH_3NH_3PbI_3$/polymeric HTMs/Au system resulted in a 12% efficiency solid state mesocopic solar cell. Although one can argue that the device deviates from a typical DSC, this works clearly opens new opportunities for the development of low cost, solution processable and high efficiency solar cells.

The main processes in a DSC system are light absorption, charge injection, electron transport and collection and electrolyte diffusion. Since 1991 most of the improvements in DSCs efficiency have been achieved through major improvements in molecular sensitizers and redox electrolytes [51]. However, directly or indirectly all of above mentioned phenomena strongly depend on the photoelectrode. In particular, the two competing processes that rule the performance of a DSC are electron transport in the mesoporous semiconductor and recombination losses in the semiconductor/electrolyte interface [52]. Both effects have been widely studied mainly using electrochemical impedance spectroscopy (EIS) but there are challenges that still remain particularly in the photoanode [31,53–60]. Consequently new photoanode structure models are needed to suppress electron recombination and to enhance light harvesting but keeping the cell′s transparency characteristics.

The ideal photoelectrode should have a high surface area to ensure high dye loading and efficient light harvesting. Even though a greater amount of electrons are photogenerated, there is also a higher probability of electrons to recombine in the interface semiconductor/electrolyte – dark current – since the pathway to get the current collector is also higher. Thus, the electron transport in the photoelectrodes plays a very important role in the electron collection efficiency since it directly influences the dark current [61]. The electron transport is essentially governed by a diffusion mechanism and it is controlled by hoping phenomena limited by the low conductivity of TiO_2 nanoparticles and their multiple grain boundaries [62]. Good electrolyte diffusion should also be guaranteed in the photoelectrode; however liquid electrolytes tend to have low viscosities, so its diffusion in the photoelectrode should not be a performance-limiting process in DSCs.

Researchers have proposed several strategies to address the transport limiting process, such as using bare 1D nano-structures composed by TiO_2, SnO, or ZnO to increase electron mobility in the photoelectrode [63,64]. Although these structures provide direct pathways for electrons to reach the collecting substrate, the inefficient dye adsorption of this type of structures do not generate enough electrons to produce high photocurrents. A common-sense

development was to mix high surface area nanoparticles with high conductive 1D structures and create hybrid photoelectrodes [65], in a way they can benefit from the advantages of each structure. Other approach consists in creating hierarchically ordered photoelectrodes with large aggregate particles composed by smaller ones [66–68]; this strategy aims to achieve high surface areas, guaranteed by small particles, and efficient electrolyte diffusion, provided by macropores created by the larger aggregates. These photoelectrodes benefit from a good light scattering effect, resulting in high performance devices. Another interesting approach was to use highly conductive host backbones to serve as charge extraction support to the high surface area nanoparticles [16,69,70]. The idea of having a 3D TCO collecting substrate has great potential because, if carefully optimized, it should be able to create a DSC where every generated electron can be collected. Following this idea of increasing the photoelectrode's conductivity, graphene has also been used in DSCs [71–75]. Benefiting from its high electrical conductivity and having a work function close to the one of TiO_2 (4.42–4.5 eV *vs* 4.5 eV, respectively), graphene should enhance electron mobility and extraction in DSCs. These various approaches are described and discussed below.

3. Nanostructured photoelectrodes

Nano science has opened the door to the development of new nanostructured materials and concepts that were not available before [76–79]. Nanostructures such as nanoparticles [77,80,81], nanowires [82–86], nanotubes [82,83,87–90], nanorods [91–93] and nanobelts [94] have been developed in the last decade for use in an array of applications in electronics, sensor devices, optoelectronics, photovoltaic and photocatalysis [78]. Nanomaterials can have very high specific surface areas even up to several hundred of $m^2\,g^{-1}$ [95,96]. Photoelectrodes of nanomaterials allow the adsorption of a large amount of sensitizer molecules in a monolayer configuration; the dye coated area relates to the photocurrent generated by the DSC device. Nanosize materials also affect the way electrons are transported through the photoelectrode structure. Unlike p–n junction solar cells, in DSCs there is no macroscopic electrostatic potential gradient in the film, fact caused by the small size of the individual colloidal particles and by the presence of concentrated electrolytes. This means that in the nanoparticle film the governing electron transport process is diffusion, contrary to the drift process seen in p–n junction solar cells for carrier separation in the presence of an electrical field [20,97].

The most common material found in DSC's photoelectrode is anatase TiO_2. This commercial metal oxide has typically surface areas between 40 and 60 m^2 and an electric resistivity in the order of 1 to $10^2\,\Omega\,cm$ [98,99].

3.1. Electron transport in nanostructure photoelectrodes

The typical electron diffusion coefficients in TiO_2 nanoparticle film, $5\times10^{-5}\,cm^2\,s^{-1}$, are found to be several orders of magnitude below single crystal (bulk) values [100–102]. The higher electron mobility and diffusion coefficients in single crystals are related to their higher electron concentrations (caused either by illumination or application of external voltage) [61,103]. The values determined for the electron diffusion coefficients point out the fact that diffusion is much slower in nanostructured materials than in single crystals; this is related to the multicrystalline nature of these structures that creates electron traps and consequently limit the lifetime of the excited electrons [61]. Although still subject of some debate [61,104,105], it is generally accepted that electron transport occurs by the combination of two phenomena: percolation through a network of sites and thermal accessibility to energy states. Therefore, morphological parameters such as porosity, surface area, pore size, particle diameter, shape and elemental crystal size and orientation within the nanostructures have an important impact on the electron diffusion coefficient but also in the energetic properties of the material, such as the distribution of trap energy or electronic concentration.

The electron transport and recombination properties can be studied by several techniques, including photocurrent/photovoltage transient techniques [106,107], intensity modulated photocurrent spectroscopy (IMPS)/intensity modulated photovoltage spectroscopy (IMVS) [100,108] and by electrochemical impedance spectroscopy (EIS) [53,109]. In particular EIS is a powerful technique for investigating the kinetic processes of DSCs. Electron transport and chemical potential in the semiconductor film, electron recombination in the photoelectrode/electrolyte interface, charge transfer at the counter electrode and the diffusion of the redox species in the electrolyte can be well distinguished based on the impedance response of the system as a function of frequency. Compared to the other techniques, EIS has the potential to allow obtaining most parameters that reflect the kinetic processes of the device. Making use of the Nyquist plots, the impedance data is fitted by an adequate equivalent circuit and the electron transport and recombination properties parameters are estimated. From these experiments three main parameters can be obtained: the recombination resistance, R_k, transport resistance, R_w and chemical capacitance of the semiconductor C_μ. In this way the electron diffusion length, L_n, and the electron lifetime, τ_n , can be determined by using the following equations [59]:

$$\tau_n = R_k C_\mu \tag{2}$$

$$L_n = L_f\sqrt{\frac{R_k}{R_w}} \tag{3}$$

$$L_n = \sqrt{\tau_n D_{eff}} \tag{4}$$

where D_{eff} is the electron diffusion coefficient and L_f is the semiconductors film thickness. Combining Eqs. (3) and (4) the effective diffusion coefficient of electrons in the semiconductor can be determined by:

$$D_{eff} = \left(\frac{R_k}{R_w}\right)\left(\frac{L_f^2}{\tau_n}\right) \tag{5}$$

Using the electron diffusion coefficient the electron transit time, τ_{tr} , can be determined by: [54,110,111]

$$\tau_{tr} = \frac{{L_f}^2}{D_{eff}} \tag{6}$$

This value indicates for how long an electron can percolate through the semiconductor before recombining with electrolyte. Before the electrons can be collected at the FTO substrate there is the possibility of recombination with the electrolyte, so an electron collecting rate at the FTO substrate should be defined [6]. Based on the two processes that rule the performance of a DSC, recombination and transport, a collection efficiency, η_{cc}, can be determined by [112]:

$$\eta_{cc} = \frac{\left[-L_n\alpha\cosh\left(\frac{L_f}{L_n}\right) + \sinh\left(\frac{L_f}{L_n}\right) + L_n\alpha e^{-\alpha L_f}\right]L_n\alpha}{\left(1-{L_n}^2\alpha^2\right)\left(1-e^{-\alpha L_f}\right)\cosh\left(\frac{L_f}{L_n}\right)} \tag{7}$$

3.2. 1D nanostructures

Considerable attention has been given to the fact that morphological features can have a clear impact in the performance of photoelectrodes in dye-sensitized solar cells, mainly in the electron transport effectiveness and the electron recombination with

electrolyte. Particular interest is given to 1D nanostructures that are believed to improve electron transport by providing direct pathways throughout the structure of the photoelectrode to the collecting substrate. The so-called 1D structures include nanotubes, nanowires and nanofibers that can be composed by several metal oxide materials such as TiO_2 ZnO or SnO_2 [63,64]. Generally, these materials have higher diffusion coefficients than non-ordered nanostructures and are meant to give electron diffusion lengths larger than film thickness. These structures can be used directly as photoelectrodes with dye molecules adsorbed in their surface – Fig. 2A – or by adding metal oxide nanoparticles to the 1D structure—Fig. 2B. Table 1 presents the diffusion coefficients as well as the correspondent cell performance characteristic values for several DSCs produced with photoelectrodes based on 1D nanostructures. The values presented in Table 1 show that 1D nanostructures present higher values of diffusion coefficients than nanoparticle based structures, meaning that generated electrons can move and reach the collecting substrate faster. However the overall DSC performance is far from the ones obtained using the conventional TiO_2 nanoparticle film. This is mainly attributed to the comparatively low internal surface area available for the adsorption of dye molecules.

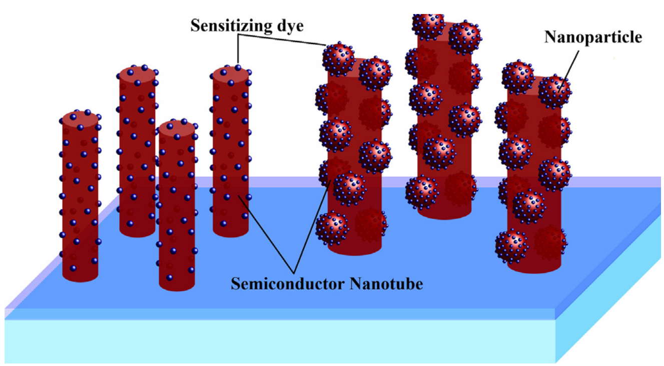


Fig. 2. (A) Schematic of 1D nanostructures with sensitizing dye adsorbed in the surface; (B) 1D nanostructures decorated with semiconductor nanoparticles.

Kang et al. [115] was one of the first authors to report good performance values with semi-transparent DSCs using a photoelectrode composed only by nanotubes. They produced nanotube arrays with external diameter of 295 nm, tube lengths of 6–15 μm and wall thickness of 21–41 nm, respectively—Fig. 3. The incorporation of this material in a DSC configuration exhibited a V_{oc} of 610 mV, a J_{sc} of 8.26 mA cm^{-2} and a fill factor of 0.70, giving an overall power conversion efficiency of 3.5%. Although these results are an improvement for nanotube-based DSC photoelectrodes, the TiO_2 nanoparticle-based DSCs still presents higher performance. As mentioned earlier, the low surface area of these types of 1D nanotube arrays can explain the relatively low efficiency of the corresponding DSC devices.

To overcome the low surface area that 1D-nanostructures have compared with nanoparticle films, some researchers combined both structures in order to take advantage of the benefits of each of them [116,117]. Gan et al. [117] created a hybrid structure combining vertically aligned ZnO nanowires (NW) with TiO_2 nanoparticles (NP) attached. ZnO has similar band gap of 3.2 eV [118] but electron mobility up to two orders of magnitude higher than TiO_2 (7×10^{-2} *vs.* 1.4 Ω cm at 25 °C, respectively) [64,99,119–121]. This makes ZnO a particularly interesting metal oxide to compete with TiO_2 in DSCs. The high value of D_{eff} of ZnO NW – based DSC substantiates that the electrons injected from excited dye molecules can travel faster and therefore are collected more efficiently – Fig. 4. However, the low value of J_{sc} in the bare ZnO electrode confirms the low surface area of these 1D aligned nanostructures. Incorporating TiO_2 NPs with inherent high surface areas in the ZnO nanowires, an increase in the current density from 1.60 to 3.54 mA cm^{-2} was obtained by these authors. The hybrid cell revealed a D_{eff} value of 6.92×10^{-4} cm^2 s^{-1} that falls between those of the bare ZnO film (2.8×10^{-3} cm^2 s^{-1}) and the TiO_2 NP electrode ($\approx5\times10^{-5}$ cm^2 s^{-1}). Actually, it is almost 15 times larger than the D_{eff} of TiO_2 NP film, showing that the

Table 1
1D nanostructured DSC performance values and diffusion coefficients.

1D nanostructure	Ref.	Cell performance				Diffusion coefficients
		η/%	J_{sc}/mA cm^{-2}	V_{oc}/mV	*FF*	D_{eff}/cm^2 s^{-1}
N719 TiO_2 NP	[113]	5.00	11.3	670	0.66	7.2×10^{-5}
Mercurochrome-sensitized ZnO nanowire	[113]	0.84	3.40	500	0.49	1.8×10^{-3}
Mercurochrome-sensitized ZnO nanowire/NP composite	[113]	2.20	6.30	610	0.58	2.1×10^{-4}
TiO_2 NP/nanotubes, 10 wt%	[64]	3.10	8.33	630	0.60	7.1×10^{-4}
TiO_2 nanorods	[114]	0.56	2.22	575	0.44	3.3×10^{-7}
TiO_2 nanorods coated with ZnO nanoparticles	[114]	0.83	3.57	545	0.43	8.0×10^{-6}
TiO_2 nanorods coated with TiO_2 nanoparticles	[114]	0.19	0.71	592	0.47	4.3×10^{-6}

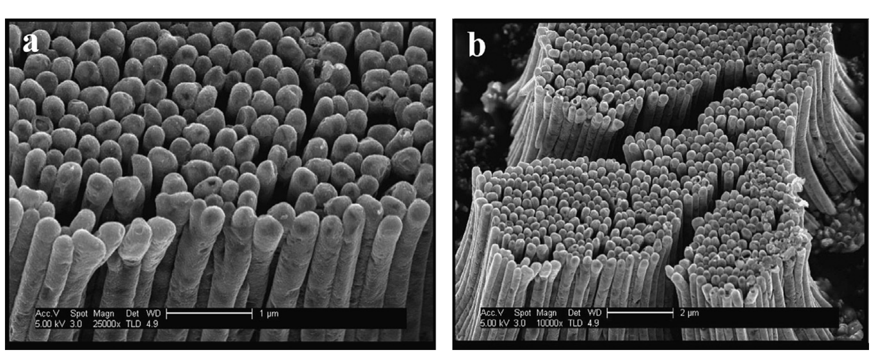
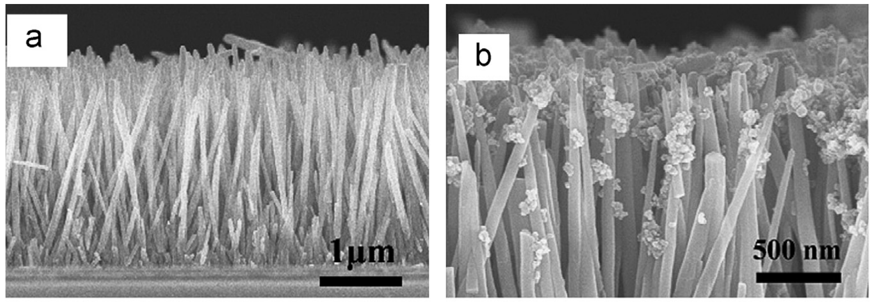


Fig. 3. Field emission-SEM images TiO_2 nanotubes [115].



Electrode	J_{sc} mA·cm2	V_{oc} / mV	FF	η /%	τ/ ms	D_{eff} / cm^2·s^{-1}
TiO_2 NP						2.52×10^{-5}
ZnO NW	1.60	610	0.40	0.39	84.03	2.80×10^{-3}
ZnO NW/TiO_2 NP	3.54	600	0.37	0.79	57.34	6.92×10^{-4}

Fig. 4. Vertically aligned nanowires: (a) without and (b) with NP attached to its surface and the correspondent DSC performance values and diffusion coefficients [117].

hybrid electrode combines the advantages of both structures: improved electron transport along the vertically aligned nanowire array and increased surface area provided by the TiO_2 NP. Nevertheless, the performance of the hybrid cell (2.2%) is still far from the nanoparticle-based DSC (5% in Table 1), mainly because the surface area provided by the hybrid solution is still low compared to a similar thickness film constituted only by nanoparticles. This fact was caused by the low coverage of the nanowires with nanoparticles as shown in Fig. 4, as well as the low thickness of the hybrid photoanode (3 μm). Nonetheless, better results can be expected if an optimization is performed to balance the ratio between the vertically aligned structures and the quantity of nanoparticles attached to its surface.

A common strategy to achieve high electron mobility but also high surface area is blending 1D nanostructures, such as TiO_2 nanotubes, with TiO_2 nanoparticles.so the photoelectrode can benefit from both the high conductive 1D nanostructure and from the high surface area available for dye adsorption—Fig. 5.

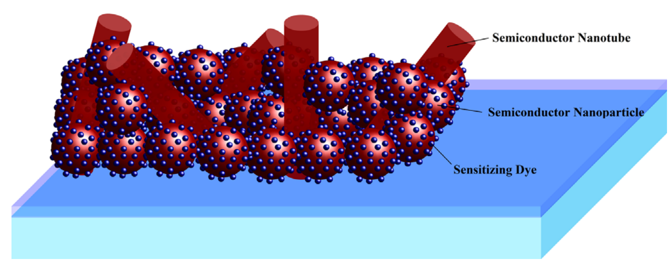


Fig. 5. Schematic of 1D nanostructures blended with metal oxide particles.

Zhong et al. [65] showed that it is possible to increase the photovoltaic performance of DSCs by blending different concentrations of TiO_2 nanotubes into a TiO_2 mesoporous film. These authors blended anodic TiO_2 nanotubes with different concentrations into a P25 based TiO_2 mesoporous film and studied the electron transport properties of the film and the recombination phenomena by electrochemical impedance spectroscopy—Fig. 6. Although this study uses a low performance TiO_2 photoelectrode as reference electrode (0 wt% of nanotubes) it provides complete EIS data allowing to withdraw important conclusions about the use of nanotubes in DSC photoelectrodes.

The same authors optimized the concentration of nanotubes blended in the photoelectrode film, increasing electron transport and slowing the electron recombination. Figs. 7 and 8 present the electron properties of DSCs with different nanotube concentrations. There is a tendency between the device's efficiency and the electron diffusion coefficient, electron diffusion length and ultimately with the electron collection efficiency. The interpretation of the diffusion length, L_n, reflects the main phenomena occurring in DSCs: the electron transport and electron recombination. For a nanotubes concentration of 10 wt%, η, η_{cc} and D_{eff} present maximum values. For a blending level of 10 wt% nanotubes dispersed in the TiO_2 particles supply shorter paths for electron transport than the disordered interconnected TiO_2 nanoparticles. For a 30 wt % nanotubes concentration, the decrease in the device efficiency is followed by the decrease of the electron diffusion coefficient and electron diffusion length due to the increase of the electron transit time. So, in this specific case, the concentration of TiO_2 nanotubes might be acting as trap centers that difficult transportation to FTO substrate. Although the TiO_2 nanotubes are more conductive than TiO_2 nanoparticles, above a certain concentration the increase of nanotubes does not result in higher electron diffusion coefficients in the film. For concentrations higher than 30 wt%, the electron lifetime increases even though the global efficiency of the device decreases. In fact, the ratio between electron lifetime and transit time becomes constant, meaning that the recombination resistance decreases at the same level of the transport resistance increases; thus the electron diffusion length remains approximately constant. Therefore, the low photocurrent density explains the efficiency decrease since the inclusion of nanotubes above 30 wt% strongly diminishes the available surface area for dye adsorption.

3.3. 3D hierarchically ordered nanostructures

The key aspects of a photoelectrode structure are large surface area, necessary to ensure high loading of dye molecules that will generate electrons, and sufficiently large pores with excellent interconnectivity for efficient electrolyte diffusion. Additionally, the defect level and the number of particle boundaries must be low to suppress electron loss by recombination with the electrolyte and allow a good electron transport to the collecting substrate. However, in a standard TiO_2 nanostructure high surface area and large pores are not compatible. Even if an increase of the surface area is important to adsorb a great amount of dye, it simultaneously decreases the average pore size, thus limiting the diffusion of the redox species in the nanostructure. As stated before, 1D vertically aligned structures solve the electron transport issue and facilitate the electrolyte diffusion throughout the photoelectrode, but do not ensure enough dye loading that could result in high performance devices. This way, 3D hierarchically pore structures are very interesting as they have several scales of pores. Indeed, such materials are of great interest as they provide high surface areas and large pore sizes at the same time: nanometer pores that

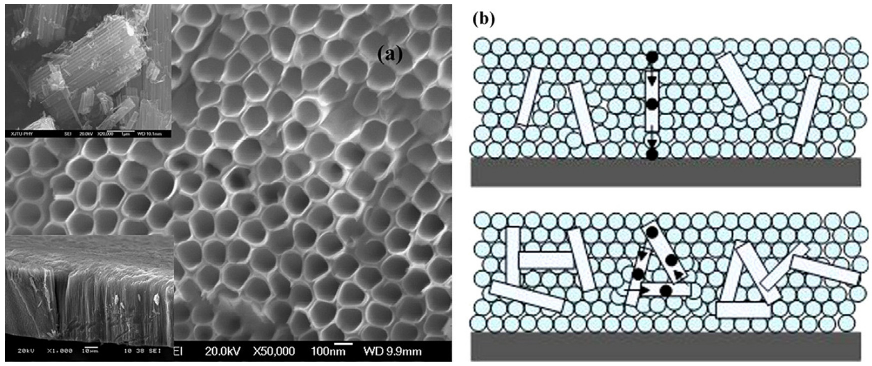


Fig. 6. (a) SEM micrograph of nanotubes sinthetized by Zhong et al. [65]; (b) schematic diagram of the electron transport in the hybrid TiO_2 film.

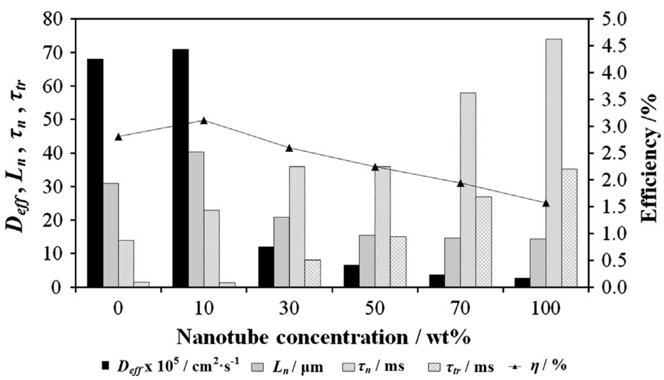


Fig. 7. Electron transport properties and DSC performance value of DSCs with different nanotube concentrations (adapted from [65]).

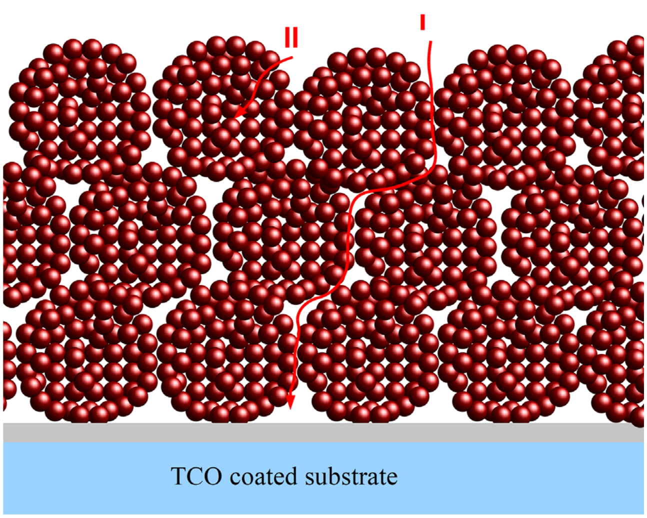


Fig. 8. Schematic representation of a hierarchical nanoparticle film, having two different scale pores: (I) meso/macropores and (II) smaller nanopores.

ensure high amount of adsorbed dye molecules – Fig. 6(II) – and large micro or mesopores that allow fast electrolyte diffusion—Fig. 6(I) [66–68].

Kim et al. [122] developed a solvothermal method for preparing crystallized TiO_2 sphere with ultrahigh surface areas up to 117.9 $m^2\,g^{-1}$ and a well-defined nanoporous structure. The strategy used for the preparation of these spheres involves a two-step approach. First, the controlled hydrolysis reaction (Eq. (8)) is carried out to form the TiO_2:

$$Ti\{OCH(CH_3)_2\}_4 + 2H_2O \rightarrow TiO_2 + 4(CH_3)_2CHOH \quad (8)$$

This reaction produces TiO_2 spheres in the amorphous phase and with a smooth surface without any pores—Fig. 9(a). The shape and size of the spheres can be controlled by the conditions of the hydrolysis reaction [122]. Then, the formed spheres are collected and washed with ethanol, and transferred to a titanium autoclave containing ethanol to conduct a hydrothermal reaction. The temperature is raised to 240 °C and held for 6 h; by this means the amorphous spherical spheres are converted to a crystallized structure with high porosity—Fig. 9(b) and (c).

The produced spheres have a diameter of 250 nm. The Brunauer–Emmett–Teller (BET) surface area of these structures was measured to be up to 117.9 $m^2\,g^{-1}$, which is 1.7 times higher than the usual surface area of a P25 film. This is an indication of the high internal surface area built in the spheres. The authors also measured the pore size distribution and found that, as expected, the spheres exhibit a bimodal pore size distribution. The N_2 adsorption–desorption isotherms showed that the TiO_2 nanoparticle film has mainly pores of 29 nm, while the spheres show pores with average pore sizes of 9 and 55 nm. The smaller pores are inside the nanoporous sphere, visible in Fig. 9(c), and they are responsible for the high surface area of the final structure. The 55 nm sized pores are originated by the interstitial voids formed by the close-packed 250 nm spheres and they are responsible for the electrolyte diffusion improvement throughout the film. The internal pore of ~9 nm did not affect the diffusion of the electrolyte probably because the diffusion length is only ≈125 nm (half of the bead diameter = 250 nm). The spheres were used to prepare TiO_2 electrodes with thicknesses in the range of 10–10.3 μm. The resulting DSCs revealed a high J_{sc} of 14.6 mA cm^{-2}, a V_{oc} of 804 mV, a FF of 0.72 and an efficiency of η = 8.44%. These values are considerable better than the results obtained for a standard nanoparticle TiO_2 film: J_{sc} of 12.7 mA cm^{-2}, a V_{oc} of 811 mV, a FF of 0.72 and an efficiency of η = 7.40%. The main difference between both types of DSCs is the short-circuit current density J_{sc} that was considerably enhanced. This increase is mainly ascribed to the increased amount of adsorbed dye molecules in semiconductor structure—140.4 μmol cm^{-2} for the cell equipped with the new photoelectrode and 122.1 μmol cm^{-2} for the conventional cell. Additionally, the produced photocurrent should also benefit from scattering effect of the larger 250 nm particles in the photoelectrode. The same authors added to the previous photoelectrode a 500 nm interfacial TiO_2 layer to decrease the electron recombination at the FTO/electrolyte interface. The TiO_2 spheres were then treated with $TiCl_4$ and, finally, the photoelectrode outer surface was coated with hollow TiO_2 nanoparticles to act as scattering layer. The final DSC device showed an excellent result of 19.6 mA cm^{-2} of J_{sc}, a V_{oc} of 766 mV, a FF of 0.69 and an efficiency of η = 10.52%.

Sauvage et al. [18] reported a single titania layer based on the same principle, using mesoporous beads of 830 nm—Figs. 10 and 11.

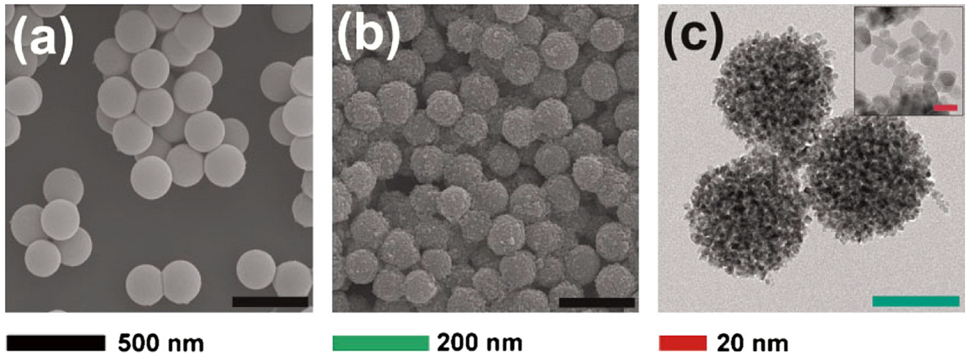


Fig. 9. SEM micrographs of the spheres synthesized by Kim et al. [122]: (a) before and (b) after the hydrothermal treatment and (c) TEM image with detail showing the porosity of the spheres.

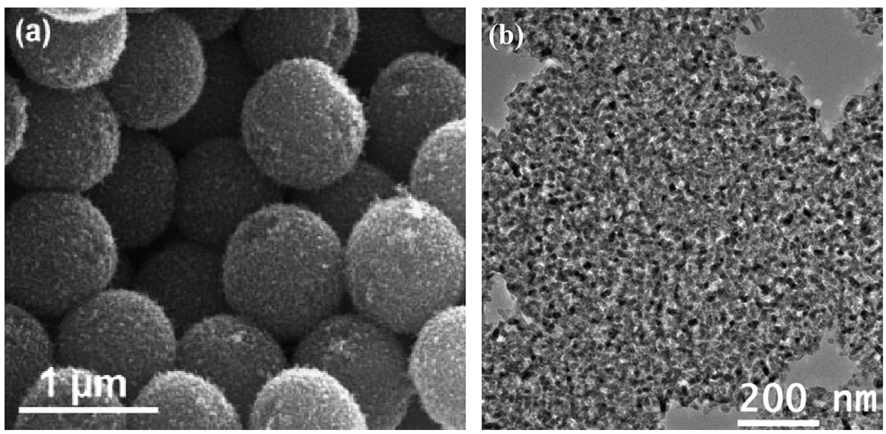


Fig. 10. SEM micrographs of the obtained beads prepared by Sauvage et al. [18] showing: (a) their close packing in the film and (b) the high mesoporosity to the core.

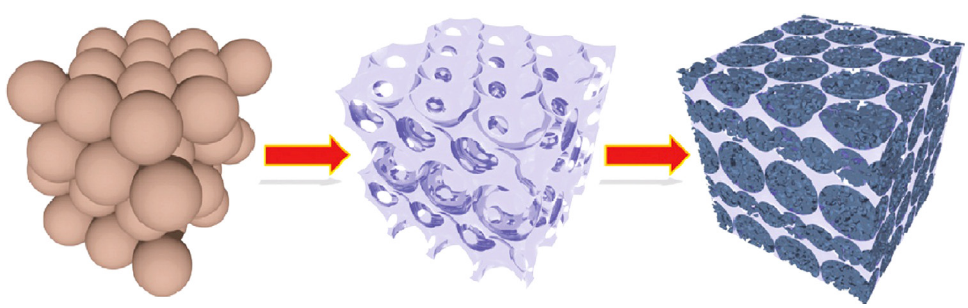


Fig. 11. Schematic representation of the preparation method of hierarchically titania frameworks. A template material, such as polystyrene spheres, is impregnated with a titania solution precursor that after the hydrolization reaction is calcinated to form the crystallized anatase backbone, adapted from [70].

The reported bead film had 89 $m^2 g^{-1}$ and a mean pore size of 23 nm. The beads showed a mesoporous structure from the surface to the core and therefore the titania nanoparticles within remain highly accessible to both chemisorption of dye molecules and electrolyte diffusion. The authors also presented evidences that inside the beads exist densely packed TiO_2 grains, having each grain contact with the neighboring ones. This aspect is responsible for the increase of electron lifetime and enhanced electron mobility, reducing the electron recombination effect with the electrolyte.

The authors reported 10.6% efficiency and an IPCE of 92% at a wavelength of 570 nm with a 12 μm single bead film and using a heteroleptic tiophene-based dye (C101 dye). However, using the standard N719 dye with the above mentioned semiconductor structure resulted in a DSC with only 8.3% efficiency. This allows concluding that the morphology and chemical nature of both nanoparticle film and dye molecule must be optimized for each other. The same authors found that the solar cells prepared with bead film showed enhanced electron lifetime, electron diffusion coefficients and diffusion length compared to a P25 film. The superior performance of the beads was mainly attributed to the close packing of grains and crystal intergrowth within the mesoporous titania beads. Similarly to what Kim et al. [122] have done, a triple layer DSC was prepared by Sauvage et al.[18], combining mesoporous beads with a transparent P25 TiO_2 interfacial layer and a light scattering layer on top of the beads, rendering an impressive J_{sc} of 19.90 mA cm^{-2}, a V_{oc} of 724 mV, a *FF* of 0.77 and an η of 11.2%. Even though the higher efficiency obtained based on

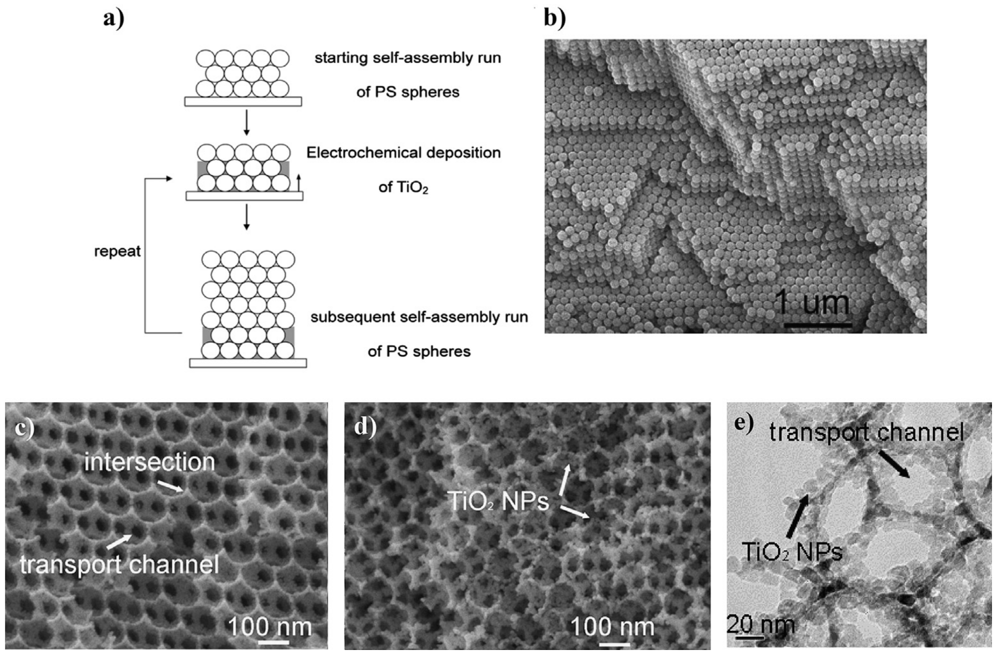


Fig. 12. (a) Schematic representation of the synthesis method of a highly ordered multi-scale nanostructure of TiO_2 proposed by Kuo et al. [125]; (b) film composed by the polystyrene opals revealing their close packing; SEM micrographs of the TiO_2 inverse opal (c) before and (d) after $TiCl_4$ treatment; (e) TEM images of the TiO_2 nanoparticle decorated inverse opal reveling the coating of the macroporous transport channels.

a complex structure it is impressive that a single 12 μm film of TiO_2 beads gave 10.6% PCE.

3.4. 3D template based backbones

Other types of hierarchically systems include structures with different length scales with different physical properties, *e.g.* systems including larger backbones with several pore and crystal sizes. It was reported to be possible to create hierarchically structures with individual control over the macro and meso structure's morphologies and dimensions, by infiltration of mesoporous amorphous silica in macroporous ceramic [123] or titania backbones [124].

This approach was later used to create fully crystalline hierarchically titania backbone, as reported by Kuo et al. [125]. This work revealed a novel multi-scale TiO_2 nanostructure, composed by a TiO_2 blocking layer at the FTO surface and an inverse opal main structure. Then, organized transport channels were created between contacting spherical voids of the TiO_2 inverse opal and TiO_2 nanoparticles coated on the spherical surfaces of the voids—Fig. 12(e). The TiO_2 inverse opal film was created by coating the blocking layer with polystyrene spheres (PS) with 100 nm of diameter. The PS template was infiltrated by electrochemical deposition of TiO_2 – Fig. 12(a) – and a close packing of PS spheres was obtained—Fig. 12(b). Afterwards, the resulting PS template was removed by calcination to obtain a crystalline inverse opal anatase scaffold opal. Then, this structure was treated with $TiCl_4$ in order to introduce TiO_2 NP into the structure and then to originate a larger surface area photoanode.

Fig. 12(c) and (d) presents SEM pictures of the anatase inverse opal structure before and after the $TiCl_4$ treatment. These figures shows TiO_2 NP of 10–15 nm attached to the backbone, as well as the transport channel openings of 30–50 nm for dye and electrolyte penetration. Similarly to the bead structures presented before, these features are believed to enhance the load of dye molecules and electrolyte diffusion within the structure. The TEM picture presented in Fig. 10(e) shows that TiO_2 NP are well crystallized and well connected, characteristics that are essential for a good electron transport through the structure. Because the NP are organized and attached to the walls of the main large pores, they have excellent access to the electrolyte. The fabricated TiO_2 nanostructure was assembled in a DSC configuration, yielding a J_{sc} of 8.2 mA cm^{-2}, a V_{oc} of 720 mV, a *FF* of 0.62 and an efficiency of η=3.7%. Although offering many potential advantages the structure proposed by Kuo et al. [125] still has low performance. Unfortunately, the authors did not present results on the surface area of the developed hierarchically structure, which may be the cause of the reported low efficiency. This issue could be addressed coating the surface area of the voids created by the PS spheres with a higher amount of TiO_2 NP.

A similar approach was reported by Mandlmeier et al. [70]. The authors created a similar highly crystalline macroporous inverse opal backbone but using polymethylmethacrylate (PMMA) spheres and a titania precursor for solution impregnation. The spheres diameter was 200 nm, two times the size of the spheres used by Kuo et al. [125]. This originated voids in the macroporous crystalline titania structure also twice the size and the intervoid connection was determined to be around 50–70 nm. The obtained scaffold can be seen in Fig. 13(a) and with detail in Fig. 13(b). After impregnation with titania precursor solution and calcination at 450 °C, the hierarchically film consists of crystalline anatase – Fig. 13(c) and (d) – with crystal size larger than 20 nm in the macroporous scaffold walls and 4–6 nm in the mesoporous walls; these values have been confirmed by HRTEM and X-ray scattering. Thus, in the same hierarchically structure there is two crystal sizes: larger sizes in the walls of the macroporous backbone and smaller ones in the mesoporous anatase filling. The authors concluded that the highly crystalline scaffold had a strong effect in the crystallization of the mesoporous filling, acting as a nucleation site for further crystallization of the initially amorphous phase [70]. Besides this, the macroporous backbone has a stabilization effect in the mesoporous material embedded in its structure, preventing pore shrinkage due to heating. Thus, the final size of the mesoporous is even 50% larger than the same material when applied on a flat surface. Mandlmeier et al. [70] also performed nitrogen adsorption experiments and determined that the macroporous scaffold exhibited a type II isotherm, typical for porous materials with macropores, and a surface area of 64 m^2 g^{-1}—Fig. 13(e)

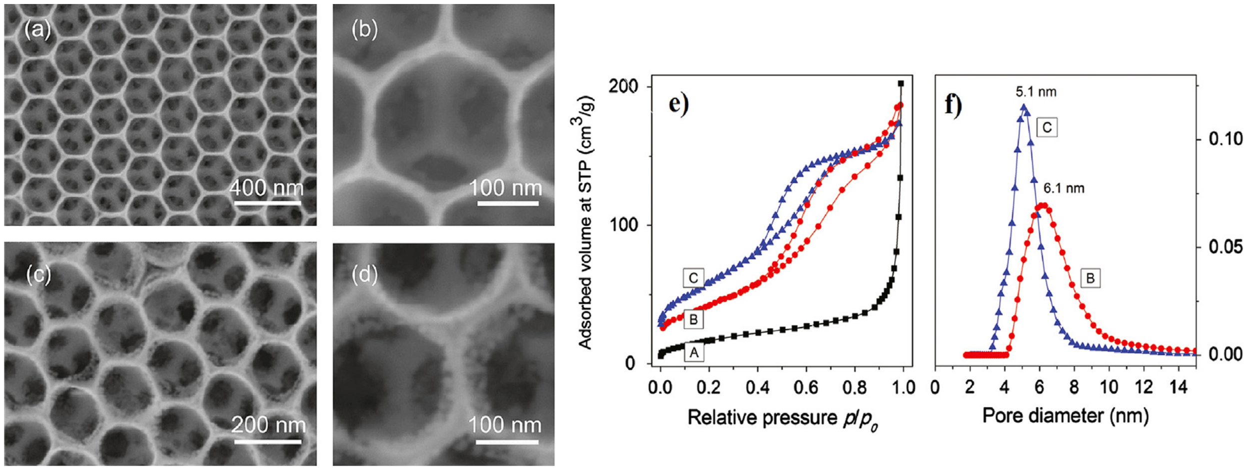


Fig. 13. SEM images of macroporous scaffold created by Mandlmeier et al. [70]: before ((a) and (b)) and after ((c) and (d)) TiO_2 NP infiltration. (e) Nitrogen adsorption/desorption isotherms (A—macroporous scaffold; B—macroporous scaffold with TiO_2 NP infiltration; C—reference mesoporous TiO_2 film); and (f) pore size distribution of the macroporous scaffold material (B) and the reference mesoporous TiO_2 (C).

curve A. After impregnation with titania solution, the hierarchically structure have a completely different adsorption behavior, exhibiting a type IV isotherm with a surface area of 154 $m^2\,g^{-1}$—Fig. 13(e) curve B. This behavior, suggests the existence of different pore sizes, ranging from micro to meso and macropores. The narrow hysteresis between the adsorption and desorption isotherms indicate a good pore distribution and its shape indicates mostly mesoporosity [126]. Although Fig. 13(e) shows very similar isotherms for the hierarchically film (isotherm B) and for a standard mesoporous film gown in a flat surface (isotherm C), the pore size distributions, shown in Fig. 13(e) and (f), are different and the average pore diameter is 6.1 nm and 5.1 nm, respectively. Additionally, a decrease in surface area from 210 $m^2\,g^{-1}$ for the mesoporous film grown in the flat surface to 174 $m^2\,g^{-1}$ for the hierarchically film was also observed. The increase in pore size up to 20% confirms the non-shrinking effect described earlier due to the nanoparticles embedded in the macroporous backbone.

Using this hierarchical titania layer as photoelectrode in a DSC the authors achieved J_{sc}=7.17 mA cm^{-2}, V_{oc}=780 mV, FF=0.71 and an efficiency of η=4.0%. This result compared to the single mesoporous titania backbone film (J_{sc} of 0.97 mA cm^{-2}, a V_{oc} of 980 mV, a FF of 0.52 and an efficiency of η=0.4%) represents an improvement of nearly 10 times. Nonetheless, the performance is very limited compared for instance to the above mentioned beads by Kim et al. [122] or by Sauvage et al. [18], who reported a performance of ~10% PCE in DSCs.

It is important to holdback that there is no clear relation between the photoelectrode surface area and the performance of the DSC. In fact, Sauvage et al. [18] used 400 nm spherical beads with 89 $m^2\,g^{-1}$ and achieved ~10% PCE; Kim et al. [122] used smaller size beads (250 nm) with larger surface area (117 $m^2\,g^{-1}$) and obtained also ~10% with similar film thickness (10–12 μm); Mandlmeier et al. [70] prepared a porous photoelectrode with the largest surface area which did not surpass 4% PCE DSC even if they have used a film with nearly half of the thickness used by the previous two authors (5.5 μm) and no additional scattering layer. On the other hand, there is a clear impact of the morphological parameters of the porous semiconductor on the DSC performance even though the relation between both is not always clear; it is still missing a deeper understanding in how the morphological features of the porous material influences the working kinetics of DSCs. Electrochemical impedance spectroscopy can play an important role in unraveling this relation but works describing a systematic electrochemical analysis on the new hierarchically photoanodes are very scarce. A very recent report by Cho et al. [69] described the preparation of a similar hierarchical structure as described by Kuo et al. [125] and Mandlmeier et al. [70]. The authors studied the influence of the template colloidal particles diameter in the final macroporous structure and its role in the electron transport properties in the final DSC device. The thickness of the electrode was changed by controlling the macroporous inverse opal support and the diameter of the mesopores was controlled using different sizes of template colloidal particles. Several complete DSC devices were prepared and Fig. 14 presents the correspondent DSC performance values, the adsorbed amount of dye in the photoelectrode and the charge transfer resistance in the TiO_2 interface, R_{ct}, (determined by EIS) as a function of the mesoscale pore diameter. It can be observed that the mesoscale pore diameter and the DSC performance are inversely proportional. This happens because the pore diameter increase corresponds to the diminishing of the surface area available for dye adsorption and, consequently, the decrease of the short-circuit current density. At this stage, the specific surface area available for

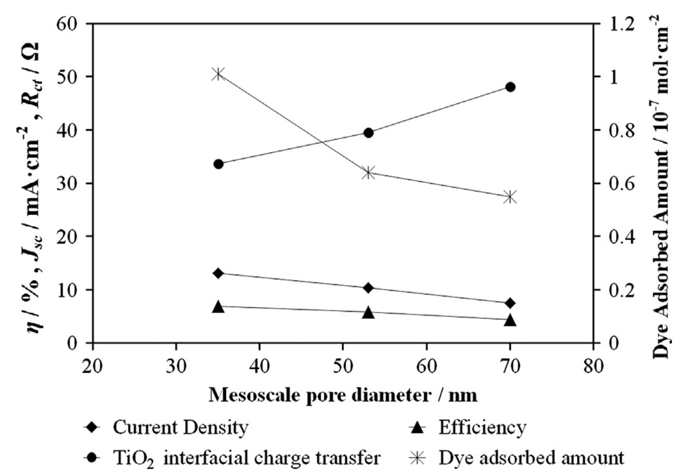


Fig. 14. DSC performance values as a function of the mesoscale pore diameter of the photoelectrode (adapted from [69]).

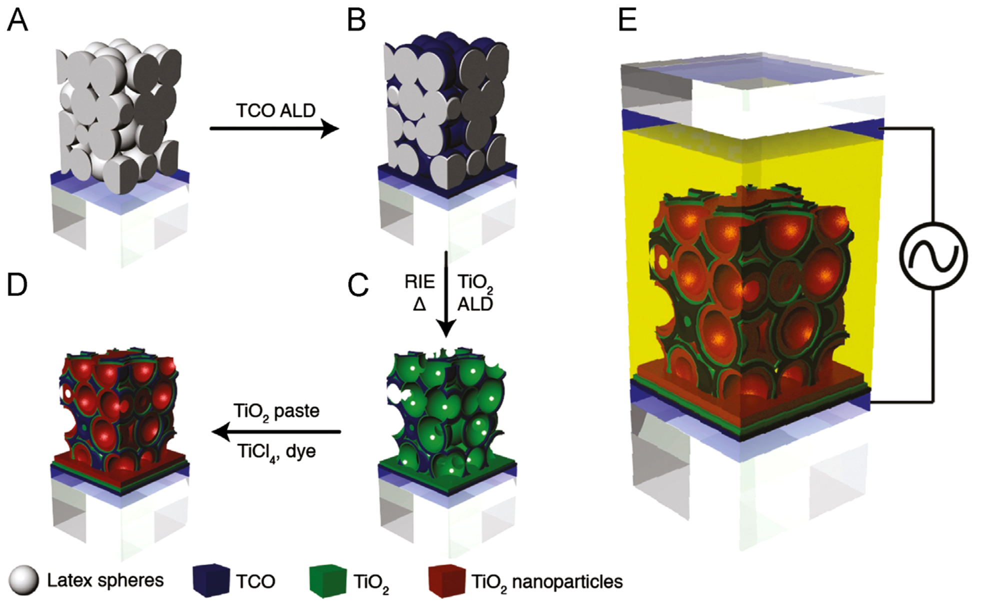


Fig. 15. Schematic diagram for the fabrication method of the 3D host passivation guest dye sensitized solar cell [16].

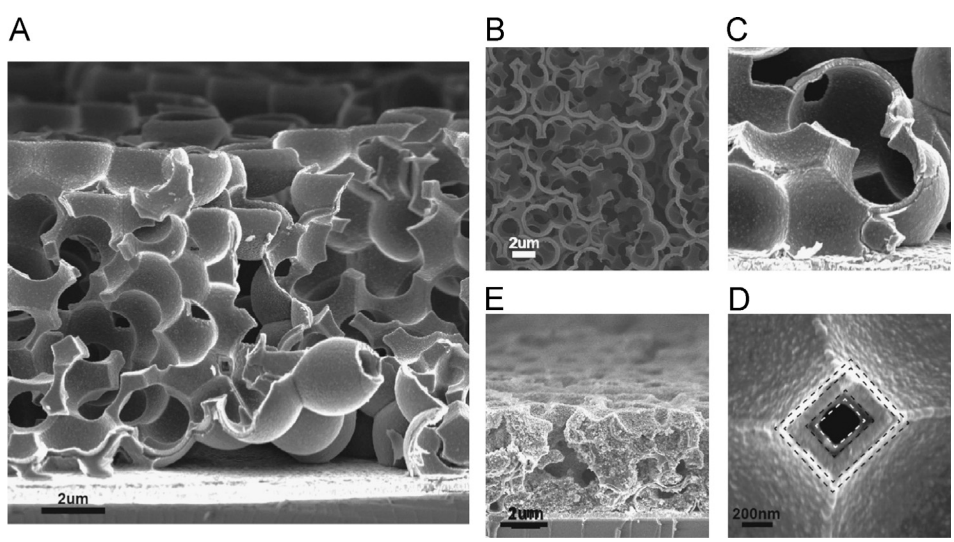


Fig. 16. SEM micrograph of a self assembled 3D Al:ZnO TiO_2 host-passivation guest DSC photoanode: (a) cross sectional view of the 3D backbone; (b) top view of the 3D backbone; (c) high-magnification micrograph showing the TiO_2 covered 3D macroporous Al:ZnO host in direct contact with the front FTO electrode; (d) high magnification micrograph showing the 3D backbone coated with dense TiO_2 inside and outside; and (e) complete photoanode after infiltration and calcination of the TiO_2 nanoparticle paste [16].

dye adsorption governs the DSC performance. Electrochemical impedance spectroscopy showed lower charge transfer resistances at the TiO_2 interfaces for smaller mesopore diameters, implying that the injection density of electrons in the conduction band of TiO_2 was higher for the DSC with 35 nm pore size photoelectrodes.

The challenge of increasing the amount of adsorbed dye molecules and increase the electron transport through the semiconductor to the FTO collecting substrate still remains. Nonetheless, hierarchically structures using template techniques are very promising because they give control over the whole pore structure of the photoelectrode. However, more kinetic data such as electron diffusion coefficients, electron diffusion lengths and ionic diffusion coefficients should be determined and correlated to the morphological features of the nanostructures in order to optimize the photoelectrode structure and maximize efficiency.

As was described throughout this review work, the increase of the specific surface area to enhance dye adsorption in TiO_2 nanostructures does not pose great challenge. What is not trivial is to increase the adsorbed amount of dye without increasing the electron/electrolyte recombination rate; indeed this should be the reason why most of the 3D strategies up to now did not produce high performance devices. The electronic loss by recombination is induced mainly by slow electron transport through the photoelectrode. Bearing this in mind, Tétreault et al. [16] followed the idea of using templating techniques to build macroporous backbones. In this case, besides using TiO_2 a thin conductive material of SnO_2 or Al/ZnO was also used to coat the template material—Fig. 15. By using polystyrene spheres they created a macroporous structure with well-defined morphological characteristics. Then, by atomic layer deposition (ALD) they created a 3D TCO macroporous scaffold. Comparing this backbone to the previously described TiO_2 ones, this shows the clear advantage of having higher electron mobility and thus to offer a 3D network for electron collection.

To avoid the electron recombination at the TCO backbone/electrolyte interface, this structure was then protected with a dense passivating TiO_2 thin layer, once again deposited by ALD. Only after the backbone was filled with 17 nm anatase nanoparticles to ensure high surface area. This approach targeted high dye loadings and injection dynamics of typical anatase nanoparticles-based DSC. Fig. 16 shows SEM micrographs of such structures where the good connection between the TCO backbone and the flat TCO substrate can be seen—Fig. 16(a) and (c). This electronic connection ensures efficient charge extraction throughout the photoelectrode. The inherent disordered structure caused by the template spheres creates an open structure that, according to the authors, only uses a small fraction of the 3D film (~10%), leaving enough volume to be filled with small TiO_2 particles with high superficial area for dye adsorption. Fig. 16(c) confirms that the TCO backbone is well coated in both sides by the dense passivation TiO_2 layer that should enable the TCO chemical stability and preventing electron recombination.

Using this new 3D material concept Tétreault et al. [16] prepared DSCs based on TiO_2, SnO_2 and Al/ZnO 3D host photoelectrodes in combination with Z907 dye. The best result was found using SnO_2 host backbone, rendering devices with J_{sc} of 10.4 mA cm^{-2}, a V_{oc} of 803 mV, a *FF* of 0.70 and an η of 5.8%. These results showed an increase of almost 100 mV when comparing with the Z907 best performing devices [127]. The electron mobility was also measured using electrochemical impedance spectroscopy and the authors found that in fact the Al/ZnO and SnO_2 films have electron diffusion coefficients six orders of magnitude higher than TiO_2 nanoparticles films (6.19 and 0.423 cm^2 s^{-1}, respectively, compared to 6×10^{-6} cm^2 s^{-1} for the TiO_2 NP film).

Table 2 compares these results with those obtained by Kuo et al. [125] and Mandlmeier et al. [70]. Despite using similar template techniques to create a TiO_2 macroporous backbone, Kuo and Mandlmeier did not report DSC efficiencies higher than 4%. The difference between their and Tétreault′s results might be in the electron diffusion coefficient. Since the three authors followed the same idea, it can be concluded that the higher performance observed is due to the higher electron mobility in the Al/ZnO and SnO_2 hosts. The findings by these authors should motivate studies to determine the influence of these highly conductive host backbones and their interaction with semiconductor particles, particularly their influence in the injection dynamics and in the overall kinetics of DSCs.

In a very recent work, Crossland et al. [128] followed this idea, and disclosed the synthesis method for mesoporous TiO_2 crystals that deliver enhanced mobility and optoelectronic device performance. This very innovative work showed that mesoporous single-crystal (MSC) semiconductor could provide long-range electronic connectivity and structural coherence. Using TiO_2 MSCs films processed under 150 °C, the authors fabricated all solid state devices with 7.3% efficiency. This result is quite remarkable, taking into account that TiO_2 nano-crystalline films are usually processed at 500 °C to improve electrical connection between nanoparticles. The synthesis process is based on a templating technique, which uses silica beads with tunable sizes from 20 to 250 nm that act as host backbone. The template material is first "seeded" with a titanium precursor, TiF_4, and only then is immersed in the reaction vessel. The reaction, hydrothermal growth of TiF_4 in the presence of hydrofluoric acid, is then carried out in the template porosity. The acid stabilizes the precursor and significantly decreases the nucleation rate, allowing the synthesis of high surface area (70 m^2 g^{-1}) single crystals of anatase TiO_2. These single crystals benefit from a much higher electron conductivity of 2.2×10^{-7} S cm^{-1} comparing to 1.5×10^{-5} S cm^{-1} measured for a TiO_2 nanoparticle sintered film at 500 °C. Obviously, with very similar surface area (70 *vs* 75 m^2 g^{-1} for TiO_2 MSCs and nanoparticles, respectively) and electrical conductivity one to two orders of magnitude higher, the mesoporous TiO_2 single crystals are an excellent candidate for replacing TiO_2 nanoparticle films in DSCs. These results, for a solid state device, surpass all the other template based techniques discussed so far, even more because they were tested with liquid electrolytes.

Table 2
DSC performance values depending on of the macroporous template backbone material.

Author	Host material	V_{oc}	J_{sc}/mA cm^{-2}	FF	Efficiency/%
Kuo et al. [125]	TiO_2	720	8.2	0.62	3.7
Mandlmeier et al. [70]	TiO_2	780	7.17	0.71	4.0
Tétreault et al. [16]	TiO_2	791	6.9	0.73	4.0
	Al/ZnO	842	7.5	0.77	4.9
	SnO_2	803	10.4	0.70	5.8

3.5. Hybrid TiO_2/graphene nanostructures

In the last couple of years graphene has attracted enormous attention because of its unique properties and array of applications [129–132]. With a theoretical surface area of 2630 m^2 g^{-1}, graphene is an ideal support material with enhanced interfacial contact even when used in small amounts [133]. Its electron mobility of 10^4 cm^2 V^{-1} [129] at room temperature means that graphene has an excellent ability to transport electrons. These facts have made it very attractive for incorporation in photocatalytic mesoporous films [134–137] and in DSC′s counter electrode [138–140], where its electrocatalytic properties have been put to use to substitute the expensive platinum catalyst. Recently, graphene has also been incorporated in DSC′s photoelectrodes—Fig. 17 [71–75]. Fourier transform infrared spectroscopy (FT-IR) experimental results of pure TiO_2 and graphene–TiO_2 hybrid films showed that Ti–O–C bonds are formed, indicating the chemical interaction between surface hydroxyl groups of TiO_2 and functional groups of graphene oxide [141]. Experimental data also shows that the presence of graphene in the TiO_2 photoelectrode also increases the total amount of dye adsorbed in the film [72,141,142]. This fact is explained by these authors based on the huge surface area of graphene that provides more anchoring sites for TiO_2. But in fact, and similarly to what happens in photocatalytic studies where there are π–π conjugations between methylene blue molecules and the aromatic rings of graphene oxide sheets, a chemical interaction between sensitizing dye and graphene might exist, helping to explain the higher amount of adsorbed dye in hybrid films [74,141,143].

Graphene is produced mainly by the chemical oxidation method resulting in graphene oxide (GO) [144,145], which can be then reduced either chemically or thermally. However, reduced graphene oxide (RGO) contains oxygen functional groups (–OH and =O) on the planes and –COOH and carbonyl groups in the periphery of the planes [138,139]. This, along with the lattice surface defects created during the exfoliation process, is believed to be responsible for the electrocatalytic behavior of graphene [146–148]. Because of GO electrocatalytic properties and its high extinction coefficient, [149] RGO should be handled carefully when used in the photoelectrode of DSCs; if not properly reduced, the remaining oxygen containing groups could promote recombination of electrons with electrolyte. In high amounts, graphene can also compete with the sensitizer molecules on light absorption and thus decrease the performance of DSCs. Therefore, the successful introduction of graphene in the photoelectrodes of DSCs depends on a careful balance between its conductive ability and electrocatalytic behavior.

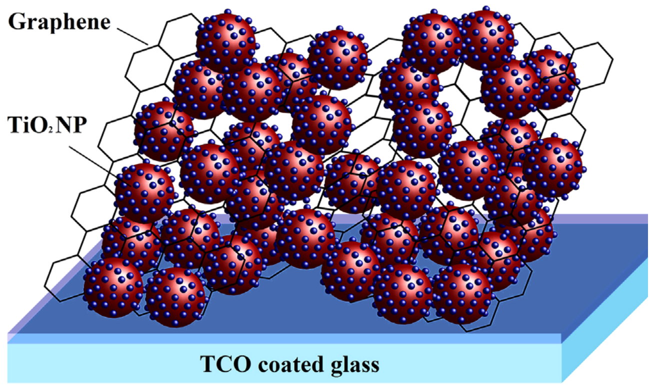


Fig. 17. Schematic representation of a TiO_2/graphene hybrid photoanode.

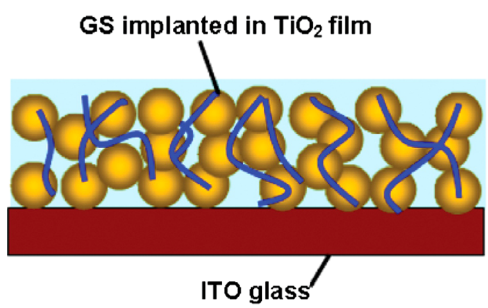


Fig. 18. Schematic representation of a TiO_2 film with GS attached (left) and SEM micrographs of the prepared film with detail to the graphene sheet attached to the TiO_2 [72].

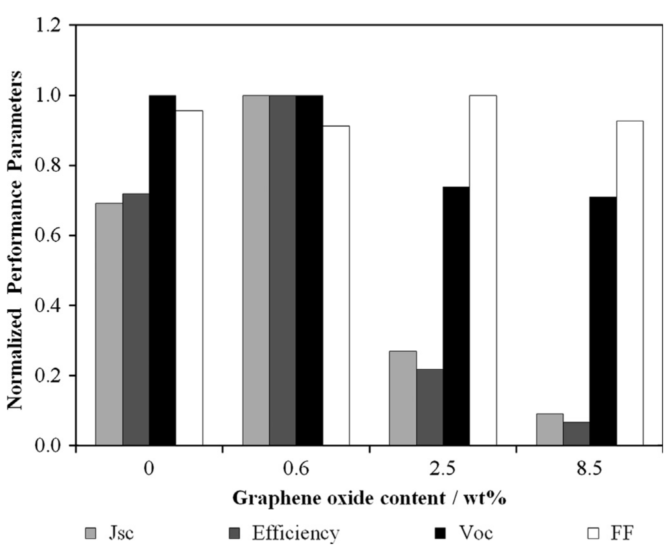


Fig. 19. TiO_2/graphene hybrid DSC normalized performance values *vs.* different graphene oxide contents present in the photoanode. Adapted from [2] Eq. (1).

Tang et al. [72] reported the development of a photoanode where exfoliated graphene sheets (GS) where attached to a TiO_2 nanoparticles matrix—Fig. 18. The authors used a molecular grafting method where the graphene sheets were chemically exfoliated and chemisorbed in the TiO_2 matrix. By controlling the oxidation time, it was possible to achieve a highly efficient electronic conductive film and thus a good attachment between the GO and the nanoparticles. In fact, the determined resistivity of a GO/TiO_2 decreased by more than two orders of magnitude from $2.1 \pm 0.9 \times 10^5$ to $3.6 \pm 0.9 \times 10^2$ Ω [72]. These authors determined that the GO provided additional and more efficient electronic transport paths but also increased the dye loading of the film, leading to a photocurrent increase.

Sun et al. [71] developed a method where graphene was dispersed using Nafion and then incorporated in TiO_2 particles by a heterogeneous coagulation particles. Because the opposite zeta potentials of P25 particles (~15 mV) and graphene (−42 mV) there is a strong electrostatic attractive force that binds the TiO_2 NP to the surface of the graphene. The authors managed to coat graphene sheets with TiO_2 resulting in a composite structure with a P25 to graphene ratio of 200:1(w/w). The DSC with P25 nanoparticles showed a J_{sc} of 5.04 mA cm^{-2} and an η of 2.70%. In the presence of 0.5 wt% of graphene the J_{sc} increased 66% to 8.38 mA cm^{-2}, resulting in an efficiency of 4.28%. The authors ascribe this enhanced performance to an increase in dye adsorption due to the creation of surface morphologies with more sites available and an extended electron lifetime since electrons travel through long mean free paths without recombining.

Yang et al. [73] successfully incorporated graphene in TiO_2 nanostructure to form 2D graphene bridges in DSCs. The authors reported an optimum result for graphene oxide content of 0.6 wt% that originated a DSC with a J_{sc} of 16.29 mA cm^{-2}, a V_{oc} of 690 mV, a *FF* of 0.62 and an η of 6.97%. This result represent an increase of 45% in the short-circuit current density and 39% in the conversion efficiency, when compared to a P25 film-based DSC, shown in Fig. 19. Comparing this result to DSCs equipped with a photoanode containing CNTs prepared by the same method and weight percentage – 0.4% – a huge difference emerges since CNT devices perform significantly worth: J_{sc} of 3.35 mA cm^{-2}, V_{oc} of 420 mV, *FF* of 0.41 and η of 0.58%. The Fermi level of a CNT is between its conduction band (CB, −4.5 eV *vs* vacuum) and its valence band. Besides, its CB is below the CB of TiO_2 (−4 eV *vs* vacuum) resulting in a decrease of the V_{oc}. In opposition, graphene is a zero band material [150] and its work function is calculated to be higher than CNT value (4.42 to 4.5 eV *vs.* vacuum) [71,151,152]. This makes graphene perfect to be introduced in the TiO_2 structure because the apparent Fermi Level is not decreased. This fact explains why in the Yang et al. results the V_{oc} was not affected by the introduction of graphene (up to 0.4 wt%) as can be seen in Fig. 19. The unaffected V_{oc} and the enhanced efficiency mean that graphene increased charge transport and partially suppressed electron recombination with the electrolyte. In higher concentrations graphene starts to compete with the sensitized TiO_2 nanoparticle for light absorption and becomes a recombination center for electrons; consequently the DSC performance is affected—Fig. 19.

4. Conclusions

Morphological features have a great impact in the performance of photoelectrodes in dye sensitized solar cells, mainly determined by changes in the electron transport effectiveness, surface area available for dye loading and pore diameter for electrolyte diffusion.

1-D nanostructures provide direct pathways for electron transport and when used as photoelectrodes improve the electron diffusion length, electron lifetime and diffusion coefficient. However, they have a fundamental disadvantage: they do not provide the necessary specific surface area for dye adsorption, resulting in DSCs with poor efficiencies (~0.5%). To overcome this problem researchers begun coating the 1D nanostructures with nanoparticles or blended 1D nanostructures in nanoparticles films for taking advantage of the characteristics of both structures: high surface area of the nanoparticles and the high electron transport characteristics of the 1-D structures. However, again relatively low efficiency values have been reported using these structures (~3%).

3D hierarchically pore structures are very interesting as they have several scales of pores. Hierarchically structured metal oxides have nanometer pores that ensure high amount of adsorbed dye molecules and large micro or mesopores, allowing rapid electrolyte diffusion. A hierarchically bead film shows enhanced electron lifetimes, electron diffusion coefficients and diffusion lengths compared to a P25 film. The superior performance of the beads, with an efficiency of ~11%, was mainly attributed to the close packing of grains and crystal intergrowth within the mesoporous titania beads. Another type of hierarchically systems includes structures with different length scales of two different physical properties, for example, pore diameter and crystal size of a larger backbone. It was reported to be possible to create hierarchically structures where there is individual control over the macro and meso structures morphologies and dimensions by infiltration of mesoporous amorphous silica in macroporous ceramics or in titania backbones. The most promising technique in this category of hierarchical films is the one proposed by Tréteault et al. that used the template idea to create a 3D TCO macroporous scaffold by atomic layer deposition. Although the relatively low efficiency (~6%) when compared NP films, the idea of creating a 3D network as electron collecting substrate has great potential. The key parameters of this structure are the compact TiO_2 layer coating of the TCO macroporous scaffold to avoid electron recombination with electrolyte and the proper filling of the structure with TiO_2 NP to achieve good adsorption of sensitizing molecules. A different idea was proposed and tested successfully by Crossland et al. In this work a mesoporous TiO_2 single crystal with high surface area and considerable higher electrical conductivity delivered a remarkable 7.3% efficient solid state solar cell. By demonstrating that MSCs displayed higher electron conductivities than nanocrystalline TiO_2, while eliminating the thermal sintering treatment, this work opened the door for a new kind of photoelectrodes in DSCs, multijunction device fabrication, temperature-sensitive substrate choice, and reduced device fabrication costs.

Finally there are some reports concerning the use of graphene in combination with TiO_2 photoelectrodes showing that graphene enhances the DSC performance when used in very low amounts (~0.5 wt%). This material promises to bring DSC′ photoelectrodes to the next level of development. The presence of graphene-bridges in a TiO_2 NP photoelectrode provides: (i) a higher electron mobility; (ii) higher amount of adsorbed dye; and (iii) decreases the electron recombination with electrolyte, improving the overall solar cell efficiency. Due to its electrocatalytic properties and high extinction coefficient, when graphene is used in higher concentrations (>0.5 wt%) and it is not properly reduced, it competes with the sensitizer on light absorption and acts as a recombination center.

The challenge of increasing both the amount of adsorbed dye molecules and the electron transport through the semiconductor to the FTO collecting substrate still remains. More kinetic data such as electron diffusion coefficients, electron diffusion lengths and ionic diffusion coefficients should be determined and correlated to the morphological features of the nanostructures to optimize the photoelectrode and maximize efficiency. This review aims to motivate other studies to investigate different materials and structures for photoelectrodes applications. Highly conductive host backbones and graphene structures are identified as promising for increasing the overall kinetics of DSCs and thus their influence and interaction with different metal oxide particles should be deeply understood.

Acknowledgements

L. Andrade and J. Maçaira are grateful to the Portuguese Foundation for Science and Technology (FCT) for their postdoctoral and PhD Grants (References: SFR/BPD/74944/2010, SFRH/BD/80449/2011, respectively). Financial support by FCT through the project SOLARCONCEPT (Reference PTDC/EQU-EQU/120064/2010 is also acknowledged.

References

[1] J Conti, PH., International Energy Outlook 2011. U.S. Energy Administration, 2011.
[2] Ciesielska, J. Global market outlook for photovolatics until 2015. European Photovoltaic Industry Association, 2011.
[3] Green MA, et al. Solar cell efficiency tables (version 39). Progress in Photovoltaics: Research and Applications 2012;20(1):12–20.
[4] Sugaya T, et al. Ultra-high stacks of InGaAs/GaAs quantum dots for high efficiency solar cells. Energy & Environmental Science 2012;5(3):6233–7.
[5] Servaites JD, Ratner MA, Marks TJ. Organic solar cells: a new look at traditional models. Energy & Environmental Science 2011;4(11):4410–22.
[6] Yella A, et al. Porphyrin-sensitized solar cells with cobalt (II/III)–based redox electrolyte exceed 12 percent efficiency. Science 2011;334(6056):629–34.
[7] Goncalves LM, et al. Dye-sensitized solar cells: a safe bet for the future. Energy & Environmental Science 2008;1(6):655–67.
[8] Nazeeruddin MK, Baranoff E, Grätzel M. Dye-sensitized solar cells: a brief overview. Solar Energy 2011;85(6):1172–8.
[9] Grätzel M. Dye-sensitized solar cells. Journal of Photochemistry and Photobiology C: Photochemistry Reviews 2003;4(2):145–53.
[10] Yum J-H, et al. Heteroleptic ruthenium complex containing substituted triphenylamine hole-transport unit as sensitizer for stable dye-sensitized solar cell. Nano Energy 2012;1(1):6–12.
[11] Kuang D, et al. High-efficiency and stable mesoscopic dye-sensitized solar cells based on a high molar extinction coefficient ruthenium sensitizer and nonvolatile electrolyte. Advanced Materials 2007;19(8):1133–7.
[12] Andrade L, et al. Influence of sodium cations of N_3 dye on the photovoltaic performance and stability of dye-sensitized solar cells. ChemPhysChem 2009;10(7):1117–24.
[13] Ribeiro F, et al. Laser assisted glass frit sealing of dye-sensitized solar cells. Solar Energy Materials and Solar Cells 2012;96(0):43–9.
[14] Wu J, et al. An all-solid-state dye-sensitized solar cell-based poly(*N*-alkyl-4-vinyl-pyridine iodide) electrolyte with efficiency of 5.64%. Journal of the American Chemical Society 2008;130(35):11568–9.
[15] Wu W, et al. Photovoltaic performance and long-term stability of quasi-solid-state fluoranthene dyes-sensitized solar cells. Renewable Energy 2010;35(8):1724–8.
[16] Tétreault N, et al. High-efficiency dye-sensitized solar cell with three-dimensional photoanode. Nano Letters 2011;11(11):4579–84.
[17] Liao J-Y, et al. High-performance dye-sensitized solar cells based on hierarchical yolk-shell anatase TiO_2 beads. Journal of Materials Chemistry 2012;22(4):1627–33.
[18] Sauvage Fdr, et al. Dye-sensitized solar cells employing a single film of mesoporous TiO_2 beads achieve power conversion efficiencies over 10%. ACS Nano 2010;4(8):4420–5.
[19] O′Regan B, Grätzel M. A low-cost, high-efficiency solar-cell based on dye-sensitized colloidal TiO_2 films. Nature 1991;353(6346):737–40.
[20] Hagfeldt A, Grätzel M. Molecular photovoltaics. Accounts of Chemical Research 2000;33(5):269–77.
[21] Andrade LR,HA, Mendes A. Dye-sensitized solar cells: an overview, in energy production and storage: inorganic chemical strategies for a warming world. In: Cabtree RH, editor. Chichester, UK: John Wiley & Sons, Ltd.; 2010. p. 53–72.
[22] Gao F, et al. Enhance the optical absorptivity of nanocrystalline TiO_2 film with high molar extinction coefficient ruthenium sensitizers for high performance dye-sensitized solar cells. Journal of the American Chemical Society 2008;130(32):10720–8.
[23] Gao F, et al. A new heteroleptic ruthenium sensitizer enhances the absorptivity of mesoporous titania film for a high efficiency dye-sensitized solar cell. Chemical Communications 2008;23:2635–7.
[24] Nazeeruddin M, Péchy P, Grätzel M. Efficient panchromatic sensitization of nanocrystalline TiO_2 films by a black dye based on a trithiocyanato–ruthenium complex. Chemistry Communications 1997;18:1705–6.
[25] Nazeeruddin M, et al. Conversion of light to electricity by cis-X2bis(2,2′-bipyridyl-4,4′-dicarboxylate)ruthenium(II) charge-transfer sensitizers ($X=Cl^-$, Br^-, I^-, CN^-, and SCN^-) on nanocrystalline titanium dioxide electrodes. Journal of the American Chemical Society 1993;115(14):6382–90.
[26] Nazeeruddin MK, et al. A high molar extinction coefficient charge transfer sensitizer and its application in dye-sensitized solar cell. Journal of Photochemistry and Photobiology A: Chemistry 2007;185(2–3):331–7.
[27] Shklover V, et al. Structure of nanocrystalline TiO_2 powders and precursor to their highly efficient photosensitizer. Chemistry of Materials 1997;9(2):430–9.
[28] Zhou W, et al. Multi-alkylthienyl appended porphyrins for efficient dye-sensitized solar cells. Dyes and Pigments 2011;91(3):404–12.
[29] Chou H-H, et al. Dipolar organic pyridyl dyes for dye-sensitized solar cell applications. Tetrahedron 2012;68(2):767–73.

[30] Teng C, et al. Two novel carbazole dyes for dye-sensitized solar cells with open-circuit voltages up to 1 V based on Br^-/Br^{3-} electrolytes. Organic Letters 2009;11(23):5542–5.
[31] Andrade L, et al. Phenomenological modeling of dye-sensitized solar cells under transient conditions. Solar Energy 2011;85(5):781–93.
[32] Chiba Y, et al. Dye-sensitized solar cells with conversion efficiency of 11.1%. Japanese Journal of Applied Physics, Part 2: Letters 2006;45(24–28):L638–L640.
[33] Nazeeruddin M, et al. Engineering of efficient panchromatic sensitizers for nanocrystalline TiO_2-based solar cells. Journal of the American Chemical Society 2001;123(8):1613–24.
[34] Martinson A, et al. New architectures for dye-sensitized solar cells. Chemistry—A European Journal 2008;14(15):4458–67.
[35] Wang M, et al. An organic redox electrolyte to rival triiodide/iodide in dye-sensitized solar cells. Nature Physics 2010;2(5):385–9.
[36] Zhang Z, et al. The 2,2,6,6-tetramethyl-1-piperidinyloxy radical: an efficient, iodine-free redox mediator for dye-sensitized solar cells. Advanced Functional Materials 2008;18(2):341–6.
[37] Bergeron B, et al. Dye-sensitized SnO_2 electrodes with iodide and pseudohalide redox mediators. Journal of Physical Chemistry B 2005;109(2):937–43.
[38] Oskam G, et al. Pseudohalogens for dye-sensitized TiO_2 photoelectrochemical cells. Journal of Physical Chemistry B 2001;105(29):6867–73.
[39] Bach U, et al. Solid-state dye-sensitized mesoporous TiO_2 solar cells with high photon-to-electron conversion efficiencies. Nature 1998;395(6702):583–5.
[40] Nusbaumer H, et al. CoII(dbbip)22+ complex rivals tri-iodide/iodide redox mediator in dye-sensitized photovoltaic cells. Journal of Physical Chemistry B 2001;105(43):10461–4.
[41] Sapp S, et al. Substituted polypyridine complexes of Cobalt(II/III) as efficient electron-transfer mediators in dye-sensitized solar cells. Journal of the American Chemical Society 2002;124(37):11215–22.
[42] Nusbaumer H, et al. An alternative efficient redox couple for the dye-sensitized solar cell system. Chemistry—A European Journal 2003;9(16):3756–63.
[43] Cameron P, et al. Electrochemical studies of the Co(III)/Co(II)(dbbip)2 redox couple as a mediator for dye-sensitized nanocrystalline solar cells. Coordination Chemistry Reviews 2004;248(13-14):1447–53.
[44] Nakade S, et al. Roles of electrolytes on charge recombination in dye-sensitized TiO_2 solar cells (2): the case of solar cells using cobalt complex redox couples. Journal of Physical Chemistry B 2005;109(8):3488–93.
[45] Burschka J, et al. Tris(2-(1*H*-pyrazol-1-yl)pyridine)cobalt(III) as p-type dopant for organic semiconductors and its application in highly efficient solid-state dye-sensitized solar cells. Journal of the American Chemical Society 2011;133(45):18042–5.
[46] Chung I, et al. All-solid-state dye-sensitized solar cells with high efficiency. Nature 2012;485(7399):486–9.
[47] Kojima A, et al. Organometal halide perovskites as visible-light sensitizers for photovoltaic cells. Journal of the American Chemical Society 2009;131(17):6050–1.
[48] Im J-H, et al. 6.5% efficient perovskite quantum-dot-sensitized solar cell. Nanoscale 2011;3(10):4088–93.
[49] Lee MM, et al. Efficient hybrid solar cells based on meso-superstructured organometal halide perovskites. Science 2012;338(6107):643–7.
[50] Heo JH, et al. Efficient inorganic-organic hybrid heterojunction solar cells containing perovskite compound and polymeric hole conductors. Nature Photonics 2013;7(6):486–91.
[51] McGehee MD. Paradigm shifts in dye-sensitized solar cells. Science 2011;334(6056):607–8.
[52] Gratzel M. Solar energy conversion by dye-sensitized photovoltaic cells. Inorganic Chemistry 2005;44(20):6841–51.
[53] Bisquert J, et al. Three-channel transmission line impedance model for mesoscopic oxide electrodes functionalized with a conductive coating. The Journal of Physical Chemistry B 2006;110(23):11284–90.
[54] Fabregat-Santiago F, et al. Influence of electrolyte in transport and recombination in dye-sensitized solar cells studied by impedance spectroscopy. Solar Energy Materials and Solar Cells 2005;87(14):117–31.
[55] Bisquert J, et al. Electron lifetime in dye-sensitized solar cells: theory and interpretation of measurements. The Journal of Physical Chemistry C 2009;113(40):17278–90.
[56] Villanueva-Cab J, Oskam G, Anta JA. A simple numerical model for the charge transport and recombination properties of dye-sensitized solar cells: a comparison of transport-limited and transfer-limited recombination. Solar Energy Materials and Solar Cells 2010;94(1):45–50.
[57] Haque SA, et al. Charge recombination kinetics in dye-sensitized nanocrystalline titanium dioxide films under externally applied bias. Journal of Physical Chemistry B 1998;102(10):1745–9.
[58] Bisquert J, Vikhrenko VS. Interpretation of the time constants measured by kinetic techniques in nanostructured semiconductor electrodes and dye-sensitized solar cells. The Journal of Physical Chemistry B 2004;108(7):2313–22.
[59] Bisquert J. Theory of the impedance of electron diffusion and recombination in a thin layer. The Journal of Physical Chemistry B 2002;106(2):325–33.
[60] Bisquert J. Theory of the impedance of charge transfer via surface states in dye-sensitized solar cells. Journal of Electroanalytical Chemistry 2010;646(1–2):43–51.
[61] Anta JA. Electron transport in nanostructured metal-oxide semiconductors. Current Opinion in Colloid and Interface Science 2012;17(3):124–31.
[62] Tetreault, N,M Gratzel. Novel nanostructures for next generation dye-sensitized solar cells. Energy & Environmental Science, 2012.
[63] Martinson ABF, et al. Electron transport in dye-sensitized solar cells based on ZnO nanotubes: evidence for highly efficient charge collection and exceptionally rapid dynamics†. The Journal of Physical Chemistry A 2009;113(16):4015–21.
[64] Tiwana P, et al. Electron mobility and injection dynamics in mesoporous ZnO, SnO_2, and TiO_2 films used in dye-sensitized solar cells. ACS Nano 2011;5(6):5158–66.
[65] Zhong P, et al. Charge transport and recombination in dye-sensitized solar cells based on hybrid films of TiO_2 particles/TiO_2 nanotubes. Journal of Alloys and Compounds 2011;509(29):7808–13.
[66] Wang Y, Caruso F. Macroporous zeolitic membrane bioreactors. Advanced Functional Materials 2004;14(10):1012–8.
[67] Zhao Y, Zhu XSJZLJCYZSYLD. TiO_2 porous electrodes with hierarchical branched inner channels for charge transport in viscous electrolytes. ChemPhysChem 2007;8(6):856–61.
[68] Fan W, et al. Hierarchical nanofabrication of microporous crystals with ordered mesoporosity. Nature Materials 2008;7(12):984–91.
[69] Cho, C-Y, Moon, JH. Hierarchical twin-scale inverse Opal TiO_2 electrodes for dye-sensitized solar cells. Langmuir, 2012.
[70] Mandlmeier B, et al. Formation of interpenetrating hierarchical titania structures by confined synthesis in inverse Opal. Journal of the American Chemical Society 2011;133(43):17274–82.
[71] Sun S, Gao L, Liu Y. Enhanced dye-sensitized solar cell using graphene-TiO [sub 2] photoanode prepared by heterogeneous coagulation. Applied Physics Letters 2010;96(8):083113.
[72] Tang Y-B, et al. Incorporation of graphenes in nanostructured TiO_2 films via molecular grafting for dye-sensitized solar cell application. ACS Nano 2010;4(6):3482–8.
[73] Yang N, et al. Two-dimensional graphene bridges enhanced photoinduced charge transport in dye-sensitized solar cells. ACS Nano 2010;4(2):887–94.
[74] Yen M-Y, et al. Preparation of graphene/multi-walled carbon nanotube hybrid and its use as photoanodes of dye-sensitized solar cells. Carbon 2011;49(11):3597–606.
[75] Kim SR, Parvez MK, Chhowalla M. UV-reduction of graphene oxide and its application as an interfacial layer to reduce the back-transport reactions in dye-sensitized solar cells. Chemical Physics Letters 2009;483(1–3):124–7.
[76] Ashby, MF, Ferreira, PJ, Schodek, DL. Chapter 1—Nanomaterials and nanotechnologies: an overview, in nanomaterials, nanotechnologies and design. 2009, Butterworth-Heinemann: Boston. p. 1–16.
[77] Edelstein, AS. Nanomaterials. In: Encyclopedia of materials: science and technology 2nd ed. KHJB Editors-in-Chief:, et al., editors; 2001, Elsevier: Oxford. p. 5916–27.
[78] Gerhard W, editor. Frontiers of nanoscience. Elsevier; 2009.
[79] Bhushan B. Springer handbook of nanotechnology. 3rd ed.Springer; 2010.
[80] Daniel L, Fedlheim CAF. Metal nanoparticles: synthesis, characterization, and applications. CRC; 2001.
[81] Solanki PR, et al. Nanostructured metal oxide-based biosensors. NPG Asia Materials 2011;3:17–24.
[82] Sattler KD. Handbook of nanophysics: nanotubes and nanowires. CRC; 2010.
[83] Sun X, Saha MS. Nanotubes, nanofibers and nanowires as supports for catalysts PEM fuel cell electrocatalysts and catalyst. In: Layers J, editor. Zhang. London: Springer; 2008. p. 655–714.
[84] Ferry DK. Nanowires in nanoelectronics. Science 2008;319(5863):579–80.
[85] Yan R, et al. Direct photonic–plasmonic coupling and routing in single nanowires. Proceedings of the National Academy of Sciences 2009;106(50):21045–50.
[86] Cheng C, Fan HJ. Branched nanowires: synthesis and energy applications. Nano Today 2012;7(4):327–43.
[87] Baughman RH, et al. Carbon nanotube actuators. Science 1999;284(5418):1340–4.
[88] Salehi-Khojin A, et al. Nonthermal current-stimulated desorption of gases from carbon nanotubes. Science 2010;329(5997):1327–30.
[89] Toma FM, et al. Efficient water oxidation at carbon nanotube–polyoxometalate electrocatalytic interfaces. Nature Chemistry 2010;2(10):826–31.
[90] Lee BY, et al. Universal parameters for carbon nanotube network-based sensors: can nanotube sensors be reproducible? ACS Nano 2011;5(6):4373–9.
[91] Wang X, et al. Synthesis of [small beta]-FeOOH and [small alpha]-Fe_2O_3 nanorods and electrochemical properties of [small beta]-FeOOH. Journal of Materials Chemistry 2004;14(5):905–7.
[92] Morber JR, et al. PLD-assisted VLS growth of aligned ferrite nanorods, nanowires, and nanobelts synthesis, and properties. The Journal of Physical Chemistry B 2006;110(43):21672–9.
[93] More AM, et al. Growth of TiO_2 nanorods by chemical bath deposition method. Applied Surface Science 2008;5:2682–7255 2008;5:2682–7.
[94] Pan ZW, Dai ZR, Wang ZL. Nanobelts of semiconducting oxides. Science 2001;291(5510):1947–9.
[95] Zhang Z, et al. Direct continuous hydrothermal synthesis of high surface area nanosized titania. Journal of Alloys and Compounds 2009;476(1–2):451–6.
[96] Chen D, et al. Synthesis of monodisperse mesoporous titania beads with controllable diameter, high surface areas, and variable pore diameters (14–23 nm). Journal of the American Chemical Society 2010;132(12):4438–44.

[97] Zhang Q, Cao G. Nanostructured photoelectrodes for dye-sensitized solar cells. Nano Today 2011;6(1):91–109.
[98] Huber B, et al. Nanocrystalline anatase TiO_2 thin films: preparation and crystallite size-dependent properties. Thin Solid Films 2005;472(1–2):114–24.
[99] Madhusudan Reddy K, Manorama SV, Reddy ARamachandra. Bandgap studies on anatase titanium dioxide nanoparticles. Materials Chemistry and Physics 2003;78(1):239–45.
[100] Dloczik L, et al. Dynamic response of dye-sensitized nanocrystalline solar cells: characterization by intensity-modulated photocurrent spectroscopy. Journal of Physical Chemistry B 1997;101(49):10281–9.
[101] Fisher AC, et al. Intensity dependence of the back reaction and transport of electrons in dye-sensitized nanocrystalline TiO_2 solar cells. The Journal of Physical Chemistry B 2000;104(5):949–58.
[102] Forro L, et al. High mobility n-type charge carriers in large single crystals of anatase (TiO_2). Journal of Applied Physics 1994;75(1):633–5.
[103] Cao F, et al. Electron transport in porous nanocrystalline TiO_2 photoelectrochemical cells. Journal of Physical Chemistry 1996;100(42):17021–7.
[104] Bisquert J. Chemical diffusion coefficient of electrons in nanostructured semiconductor electrodes and dye-sensitized solar cells. The Journal of Physical Chemistry B 2004;108(7):2323–32.
[105] Bisquert J, Mora-Sero In. Simulation of steady-state characteristics of dye-sensitized solar cells and the interpretation of the diffusion length. The Journal of Physical Chemistry Letters 2009;1(1):450–6.
[106] van de Lagemaat J, Frank AJ. Nonthermalized electron transport in dye-sensitized nanocrystalline TiO_2 films: transient photocurrent and random-walk modeling studies. The Journal of Physical Chemistry B 2001;105(45):11194–205.
[107] Kopidakis N, et al. Transport-limited recombination of photocarriers in dye-sensitized nanocrystalline TiO_2 solar cells. The Journal of Physical Chemistry B 2003;107(41):11307–15.
[108] Chen C, Wang M, Wang K. Characterization of polymer/TiO_2 photovoltaic cells by intensity modulated photocurrent spectroscopy. The Journal of Physical Chemistry C 2009;113(4):1624–31.
[109] Wang Q, et al. Characteristics of high efficiency dye-sensitized solar cells. Journal of Physical Chemistry B 2006;110:25210–21.
[110] Fan K, et al. Effects of tetrabutoxytitanium on photoelectrochemical properties of plastic-based TiO_2 film electrodes for flexible dye-sensitized solar cells. Journal of Power Sources 2011;196(5):2939–44.
[111] Hagfeldt A, et al. Dye-sensitized solar cells. Chemical Reviews 2010;110(11):6595–663.
[112] Bertoluzzi L, Ma S. On the methods of calculation of the charge collection efficiency of dye sensitized solar cells. Physical Chemistry Chemical Physics 2013;15(12):4283–5.
[113] Ku C-H, Wu J-J. Electron transport properties in ZnO nanowire array/nanoparticle composite dye-sensitized solar cells. Applied Physics Letters 2007;91(9):093117.
[114] Samadpour M, et al. Charge transport properties in nanocomposite photoanodes of DSSCs: crucial role of electronic structure. European Physical Journal-Applied Physics 2012;57:2.
[115] Kang T-S, et al. Fabrication of highly-ordered TiO_2 nanotube arrays and their use in dye-sensitized solar cells. Nano Letters 2009;9(2):601–6.
[116] Wong DK-P, et al. Enhancing electron collection efficiency and effective diffusion length in dye-sensitized solar cells. Chemphyschem 2009;10(15):2698–702.
[117] Gan X, et al. ZnO nanowire/TiO_2 nanoparticle photoanodes prepared by the ultrasonic irradiation assisted dip-coating method. Thin Solid Films 2010;518(17):4809–12.
[118] Zhang R, et al. Mesoporous titania: from synthesis to application. Nano Today 2012;7(4):344–66.
[119] Moezzi A, McDonagh AM, Cortie MB. Zinc oxide particles: synthesis, properties and applications. Chemical Engineering Journal 2012;185–186(0):1–22.
[120] Hasiguti RR, Yagi E. Electrical conductivity below 3 K of slightly reduced oxygen-deficient rutile TiO_{2-x}. Physical Review B: Condensed Matter 1994;49(11):7251–6.
[121] Ji L-c, et al. Optical and electrical properties of zinc oxide/indium/zinc oxide multilayer structures. Thin Solid Films 2011;519(11):3789–91.
[122] Kim YJ, et al. Formation of highly efficient dye-sensitized solar cells by hierarchical pore generation with nanoporous TiO_2 spheres. Advanced Materials 2009;21(36):3668–73.
[123] Costacurta S, et al. Hierarchical porosity components by infiltration of a ceramic foam. Journal of the American Ceramic Society 2007;90(7):2172–7.
[124] Angelomé PC, Fuertes MC, Soler-Illia GJAA. Multifunctional, multilayer, multiscale: integrative synthesis of complex macroporous and mesoporous thin films with spatial separation of porosity and function. Advanced Materials 2006;18(18):2397–402.
[125] Kuo C, Lu S. Fabrication of a multi-scale nanostructure of TiO_2 for application in dye-sensitized solar cells. Nanotechnology 2008;19(9):095705.
[126] Shao G-S, et al. Exotemplating synthesis of nitrogen-doped carbon materials with hierarchically porous structure and their application for lysozyme adsorption. Chemical Engineering Journal 2011;174(1):452–60.
[127] Cao Y, et al. Dye-sensitized solar cells with a high absorptivity ruthenium sensitizer featuring a 2-(hexylthio)thiophene conjugated bipyridine. The Journal of Physical Chemistry C 2009;113(15):6290–7.
[128] Crossland EJW, et al. Mesoporous TiO_2 single crystals delivering enhanced mobility and optoelectronic device performance. Nature 2013;495(7440):215–9.
[129] Novoselov KS, et al. Electric field effect in atomically thin carbon films. Science 2004;306(5696):666–9.
[130] Wu Z-S, et al. Graphene/metal oxide composite electrode materials for energy storage. Nano Energy 2012;1(1):107–31.
[131] Yang S, Feng X, Müllen K. Sandwich-like, graphene-based titania nanosheets with high surface area for fast lithium storage. Advanced Materials 2011;23(31):3575–9.
[132] Craciun MF, et al. Tuneable electronic properties in graphene. Nano Today 2011;6(1):42–60.
[133] Peigney A, et al. Specific surface area of carbon nanotubes and bundles of carbon nanotubes. Carbon 2001;39(4):507–14.
[134] Robin IC, et al. Doping in homoepitaxial ZnO films: effect of intentional and unintentional impurities on the optical and the electrical properties. Journal of the Korean Physical Society 2008;53(5):2888–92.
[135] Ng YH, et al. To what extent do graphene scaffolds improve the photovoltaic and photocatalytic response of TiO_2 nanostructured films? The Journal of Physical Chemistry Letters 2010;1(15):2222–7.
[136] Bell NJ, et al. Understanding the enhancement in photoelectrochemical properties of photocatalytically prepared TiO_2-reduced graphene oxide composite. The Journal of Physical Chemistry C 2011;115(13):6004–9.
[137] Du J, et al. Hierarchically ordered macro − mesoporous TiO_2 − graphene composite films: improved mass transfer, reduced charge recombination, and their enhanced photocatalytic activities. ACS Nano 2010;5(1):590–6.
[138] Zhang DW, et al. Graphene-based counter electrode for dye-sensitized solar cells. Carbon 2011;49(15):5382–8.
[139] Cruz R, Pacheco Tanaka DA, Mendes A. Reduced graphene oxide films as transparent counter-electrodes for dye-sensitized solar cells. Solar Energy 2012;86(2):716–24.
[140] Yeh M-H, et al. A low-cost counter electrode of ITO glass coated with a graphene/Nafion® composite film for use in dye-sensitized solar cells. Carbon 2012;50(11):4192–202.
[141] Nguyen-Phan T-D, et al. The role of graphene oxide content on the adsorption-enhanced photocatalysis of titanium dioxide/graphene oxide composites. Chemical Engineering Journal 2011;170(1):226–32.
[142] Tang B, Hu G. Two kinds of graphene-based composites for photoanode applying in dye-sensitized solar cell. Journal of Power Sources 2012;220:95–102.
[143] Liu Z, et al. PEGylated nanographene oxide for delivery of water-insoluble cancer drugs. Journal of the American Chemical Society 2008;130(33):10876–7.
[144] Li D, et al. Processable aqueous dispersions of graphene nanosheets. Nature Nanotechnology 2008;3(2):101–5.
[145] Titelman GI, et al. Characteristics and microstructure of aqueous colloidal dispersions of graphite oxide. Carbon 2005;43(3):641–9.
[146] Murakami TN, Grätzel M. Counter electrodes for DSC: application of functional materials as catalysts. Inorganica Chimica Acta 2008;361(3):572–80.
[147] Imoto K, et al. High-performance carbon counter electrode for dye-sensitized solar cells. Solar Energy Materials and Solar Cells 2003;79(4):459–69.
[148] Kavan L, Yum JH, Grätzel M. Optically transparent cathode for dye-sensitized solar cells based on graphene nanoplatelets. ACS Nano 2010;5(1):165–72.
[149] Gray A, et al. Optical detection and characterization of graphene by broadband spectrophotometry. Journal of Applied Physics 2008;104(5):053109.
[150] Freitag M. Graphene: Nanoelectronics goes flat out. Nature Nanotechnology 2008;3(8):455–7.
[151] Czerw R, et al. Substrate-interface interactions between carbon nanotubes and the supporting substrate. Physical Review B: Condensed Matter 2002;66(3):033408.
[152] Wilder JWG, et al. Electronic structure of atomically resolved carbon nanotubes. Nature 1998;391(6662):59–62.